Journal of Fluid Mechanics
http://journals.cambridge.org/FLM

Additional services for ***Journal of Fluid Mechanics:***

Email alerts: Click here
Subscriptions: Click here
Commercial reprints: Click here
Terms of use : Click here

Nonlinear Rossby adjustment in a channel: beyond Kelvin waves

Albert J. Hermann, Peter B. Rhines and E. R. Johnson

Journal of Fluid Mechanics / Volume 205 / August 1989, pp 469 - 502
DOI: 10.1017/S0022112089002119, Published online: 26 April 2006

Link to this article: http://journals.cambridge.org/abstract_S0022112089002119

How to cite this article:
Albert J. Hermann, Peter B. Rhines and E. R. Johnson (1989). Nonlinear Rossby adjustment in a channel: beyond Kelvin waves. Journal of Fluid Mechanics, 205, pp 469-502 doi:10.1017/S0022112089002119

Request Permissions : Click here

CAMBRIDGE JOURNALS

Downloaded from http://journals.cambridge.org/FLM, IP address: 144.82.107.45 on 30 Oct 2012

J. Fluid Mech. (1989), *vol.* 205, *pp.* 469–502
Printed in Great Britain

Nonlinear Rossby adjustment in a channel: beyond Kelvin waves

By ALBERT J. HERMANN[1]† PETER B. RHINES[1] AND E. R. JOHNSON[2]

[1] School of Oceanography, WB-10, University of Washington, Seattle, WA 98195, USA
[2] Department of Mathematics, University College London, WC1E 6BT, UK

(Received 14 June 1988 and in revised form 22 February 1989)

Nonlinear advective adjustment of a discontinuity in free-surface height under gravity and rotation is considered, using the method of contour dynamics. After linear wave-adjustment has set up an interior jet and boundary currents in a wide ($\gg$ one Rossby radius) channel, fluid surges down-channel on both walls, rather than only that wall supporting a down-channel Kelvin wave. A wedgelike intrusion of low potential vorticity fluid on this wall, and a noselike intrusion of such fluid on the opposite wall, serve to reverse the sign of relative vorticity in the pre-existing currents. For narrower channels, a coherent boundary-trapped structure of low potential vorticity fluid is ejected at one wall, and shoots ahead of its parent fluid. The initial tendency for the current to concentrate on the 'right-hand' wall (the one supporting a down-channel Kelvin wave in the northern hemisphere) is defeated as vorticity advection shifts the maximum to the left-hand side. Ultimately fluid washes downstream everywhere across even wide channels, leaving the linearly adjusted upstream condition as the final state. The time necessary for this to occur grows exponentially with channel width. The width of small-amplitude boundary currents in linear theory is equal to Rossby's deformation radius, yet here we find that the width of the variation in velocity and potential vorticity fields deviates from this scale across a large region of space and time. Comparisons of the contour dynamics solutions, valid for small amplitude, and integration of the shallow-water equations at large amplitude, show great similarity. Boundary friction strongly modifies these results, producing fields more closely resembling the linear wave-adjusted state. Observed features include those suggestive of coastally trapped gravity currents. Analytical results for the evolution of vorticity fronts near boundaries are given in support of the numerical experiments.

1. Introduction

Rossby (1937, 1938) was the first investigator to consider in detail the adjustment to gravitational equilibrium of an unbounded rotating fluid, and now the general problem bears his name. Blumen's (1972) extensive review addressed the general problem of agestrophic initial states. Gill (1976, 1982) explicitly considered the gravitational adjustment of a step discontinuity in surface height and examined the energetics of this adjustment. Starting with the linearized shallow-water equations, he derived both a wave equation and the expression for potential vorticity

† Present address: Department of Physical Oceanography, Woods Hole Oceanographic Institution, Woods Hole, MA 02543, USA.

conservation, which together revealed the evolution and structure of the geostrophically adjusted state. Essentially this state consists of a jet centred on the original position of the height (and potential vorticity) discontinuity. Of the total potential energy lost from this region during the adjustment process, only one-third is converted into kinetic energy of the geostrophic jet. The remainder is lost as inertio-gravity waves (Poincaré waves), which move steadily outward from the initial discontinuity. This partition varies with the mix of Fourier components in the initial field (Killworth 1987; Middleton 1987).

Gill (1976) also considered the related problem of geostrophic adjustment to a height discontinuity in the presence of boundaries which lie perpendicularly to that discontinuity. Such gravitational adjustment in a rotating channel (henceforth termed the 'Gill adjustment problem') involves not only the Poincaré waves of the unbounded case, but also Kelvin waves trapped against each boundary. Combined Kelvin/Poincaré fronts move out from the initial discontinuity, setting up source–sink flows (in this case, boundary currents) in their wake (figure 1). The linearly adjusted jet is situated at the left-hand wall in the up-channel region of initially thicker fluid, crosses over at the position of the initial discontinuity, and is located on the right-hand wall down channel from that location (here 'right' and 'left' apply to an observer looking down the channel from the region of high surface elevation, in the northern hemisphere). The relative vorticity of the boundary currents is just that provided by the wave of depression moving upstream (which shortens planetary vortex lines, making negative vorticity) and the wave of elevation moving downstream (which stretches vortex lines to make positive vorticity). This idealization in which Kelvin waves establish pathways for drainage flows, is the basis of a wide variety of adjustment problems. The analogous determination of linear source–sink circulations by wave group–velocity arguments is the basis of a large variety of geophysical flow problems (e.g. internal waves and barotropic Rossby waves: Lighthill 1967; topographic shelf waves: Csanady 1976; topographic waves: Johnson 1985, Gill *et al.* 1986; boundary and equatorial Kelvin waves, and baroclinic Rossby waves: Kawase 1987).

In the non-diffusive Gill adjustment problem, Kelvin waves of elevation and depression serve to flatten the down-channel pressure gradients which initially exist at each wall; for a geostrophically adjusted flow, no such gradients are possible, for they would imply flow through each wall. The constant values of surface height thus attained on each wall set a constant value for total down-channel mass flux at any cross-section of the channel.

This linear solution (henceforth termed the 'Gill solution') to the adjustment problem will hold only so long as fluid excursions are very small, i.e. so long as potential vorticity is conserved everywhere in an Eulerian sense. However, once fluid has moved across the initial location of the discontinuity in height and potential vorticity, this linear conservation law is violated. Indeed, the potential vorticity field of the Gill solution will be of the wrong sign for those areas where particles have crossed the position of the initial discontinuity. The results of this sudden change are difficult to predict in detail. But we anticipate that the negative vorticity of the fluid approaching $x = 0$, if it were to overshoot in making its right-hand turn, would (with its boundary image) tend to self-advect down the left-hand wall. Conversely if a 'nose' of fluid with negative vorticity were to flood down the right-hand wall, its self advection with its boundary image would tend to slow its advance. One might argue that the new fluid will permanently carry on down the right-hand wall, with its maximum velocity shifted away from the boundary to express its negative vorticity.

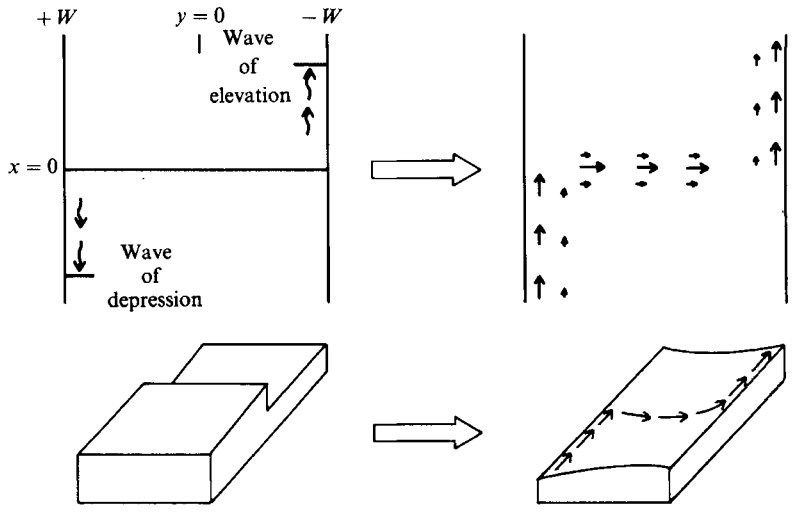

FIGURE 1. Linear set-up of the geostrophically adjusted flow in a channel. Poincaré/Kelvin fronts move out from an initial discontinuity, setting up an antisymmetric pattern of boundary currents.

But this resolution, to be permanent, would require a vortex sheet between the jet and the quiescent interior, positive vorticity for which there is no source. The possibility of a major change in flow path led us to develop numerical solutions for the vorticity dynamics of these advective changes.

For the nonlinear (advectively driven) adjustment problem, we must specifically conserve potential vorticity for all fluid parcels. Here we divide the full adjustment problem into two distinct phases: the linear phase where Kelvin and Poincaré fronts set up boundary and interior jets, and a much slower nonlinear phase where advection of fluid rearranges the initial pattern of potential vorticity. The separate treatment of these two phases presumes that the linear set-up is complete (i.e. the Kelvin and Poincaré waves have moved infinitely far off from the origin) before the nonlinear adjustment begins. Such a timescale separation becomes more and more accurate as the amplitude of the initial step discontinuity becomes smaller. Wave steepening and breaking become unimportant in the same limit. Nonetheless, as will be shown later, the basic pattern of evolution holds, even for initial disturbances of finite amplitude. Since the nonlinear phase still entails a pattern of potential vorticity which is piecewise continuous, the ideal method of solution for small amplitudes is that of contour dynamics (Zabusky, Hughes & Roberts 1979), which has been employed here.

The nonlinear adjustment problem with boundaries is relevant to many physical situations in the oceans and atmosphere. A most obvious example is the 'dam break' problem for ocean straits, where the dynamical evolution of along-straight variations in pressure is sought. Localized mixing can create along-strait pressure gradients which will subsequently evolve, undergoing both gravitational and advective adjustment. For the atmosphere, the nonlinear adjustment problem bears considerable relevance to the evolution of alongshore variations in the height of the marine layer in the presence of a coastal mountain barrier, which has been studied at a variety of locations (e.g. Gill 1977*a*; Baines 1980; Mass & Albright 1987; Beardlsey *et al.* 1987; Dorman 1987; Hermann *et al.* 1989). Such alongshore variations in layer height, which can be set up initially by synoptic-scale dynamics, may propagate as Kelvin waves, steepen and break into bores, and, when the

variation in height is strong enough, take on the characteristics of a coastally trapped gravity current. The problem described in this communication, in the limit of infinite channel width, serves as a useful analogue to this adjustment process.

Certain wind-forced adjustments in the coastal ocean could also exhibit features similar to those reported here. A broad, long patch of alongshore wind, with negative curl (increasing wind strength offshore) and blowing in the direction that Kelvin waves propagate, would produce a convergence of fluid and hence a thickening of the mixed layer far out beyond the coastal boundary. Such a broad hump of coastal water would possess alongshore pressure gradients near the wall, due to the forcing of Kelvin waves there. A boundary current would be established by those free waves moving out from the forcing region, which would serve to advect the wind-forced fluid along the coast into a region of higher ambient potential vorticity. This could produce results similar to those described here for the advective adjustment phase of the initially quiescent fluid near the 'right-hand' wall.

In this paper we emphasize the role of vorticity dynamics in setting the flow near boundaries. The linearly adjusted state represents one dynamical extreme for this problem, whereas steady hydraulics (e.g. Gill 1977*b*) represents another. The nonlinear dynamics considered here use the former as their starting point, and describe the approach toward the latter: a steady nonlinear flow in a rotating channel. This approach should be especially slow in those channels much wider than one deformation radius. In between linear adjustment and steady hydraulics lies a relatively obscure dynamical regime, whose study may help bridge the gap between linear Kelvin waves (which move no fluid) and boundary-trapped gravity currents (whose wave and fluid fronts are coincident). Stern (1985, 1986, 1987*a*, 1987*b*) has been particularly active in the application of contour dynamics to nonlinear evolution, his applications centring on the growth of wavy disturbances on Gulf Stream jets, coastal currents, and large-scale eddies.

Section 2 describes the set-up of the problem and the method of solution. Section 3 describes the results of the contour dynamical technique for a range of channel widths. Section 4 compares these results with current theory, simpler cases, and larger amplitudes. Section 5 presents the conclusions.

2. Equations of motion

Consider a fluid of average depth H initially at rest relative to the frame of reference S of a rectilinear flat-bottomed channel of width $2W$ rotating with angular velocity $\frac{1}{2}f$ about a vertical axis. Take Cartesian axes Ox^*y^*z with Oz^* vertical and Ox^* along-channel. Denote the instantaneous surface elevation by η^* and let the initial elevation be given by

$$\eta^* = H(1-\epsilon \operatorname{sgn} x), \tag{2.1}$$

where $0 < \epsilon \ll 1$. It is shown below that ϵ gives the ratio of advective to wave timescales. Take the aspect ratio H/L of the flow to be sufficiently small that the subsequent motion of the fluid is described by the nonlinear shallow water equations, namely

$$u_t + \epsilon(uu_x + vu_y) - v = -\eta_x, \tag{2.2}$$

$$v_t + \epsilon(uv_x + vv_y) + u = -\eta_y, \tag{2.3}$$

$$\eta_t + u_x + v_y + \epsilon[(u\eta)_x + (v\eta)_y] = 0. \tag{2.4}$$

Here η is the non-dimensional scaled surface displacement given by $\eta^* = H(1+\epsilon\eta)$,

t is the time scaled on f^{-1}, horizontal lengths are scaled on the Rossby radius, $(gH)^{\frac{1}{2}}/f$, and (u, v) are the horizontal velocity components scaled on $\epsilon(gH)^{\frac{1}{2}}$, small compared to the long-wave speed. The boundary conditions on the flow are

$$v = 0 \quad (y = \pm W, \quad t > 0), \tag{2.5}$$

$$u = v = 0, \quad \eta = -\operatorname{sgn} x \quad (|y| \leqslant W, \quad t = 0), \tag{2.6}$$

$$u, v \to 0 \quad (|y| \leqslant W, \quad |x| \to \infty, \quad t > 0), \tag{2.7}$$

where $W = fL/(gH)^{\frac{1}{2}}$ is the channel half-width expressed in Rossby radii. The behaviour of system (2.2)–(2.7) is determined entirely by the two non-dimensional parameters ϵ and W. Equations (2.2)–(2.4) can be arranged to show that the non-dimensional potential vorticity

$$Q' = \frac{1+\epsilon\zeta}{1+\epsilon\eta}, \tag{2.8}$$

is conserved following fluid particles. Here $\zeta = v_x - u_y$ is the vertical component of the relative vorticity.

We consider system (2.2)–(2.7) for small ϵ, yet with fully nonlinear evolution emerging over times of order ϵ^{-1}. The initial adjustment takes place over the inertial time scale f^{-1} and is governed by (2.2)–(2.7) with the nonlinear terms absent. The conservation of Q' then becomes the requirement that Q' retains its initial value, i.e. to leading order

$$\zeta - \eta = \operatorname{sgn} x \quad (t > 0). \tag{2.9}$$

Gill (1976) discussed fully the radiation of Poincaré and Kelvin waves, presenting a closed-form solution of the complete time-dependent wave-adjustment problem. The present analysis is concerned with the subsequent advective adjustment and so requires only the final steady-state surface displacement at the walls from the wave problem. This follows directly from information propagation arguments. Introduce the advective time $\tau = \epsilon t$, the time taken for a particle to travel one Rossby radius (*vs.* t, the timescale for a gravity wave to travel the same distance). Then in the present limit (2.2), (2.3) give the geostrophic relations

$$u = -\eta_y, \quad v = \eta_x. \tag{2.10}$$

The boundary condition (2.5) becomes

$$\eta_x = 0 \quad (y = \pm W, \quad \tau > 0), \tag{2.11}$$

conservation of potential vorticity is given by

$$Q_\tau + J(\eta, Q) = 0 \tag{2.12}$$

where $J(\eta, Q) = \eta_x Q_y - \eta_y Q_x$ and Q is the leading-order potential vorticity,

$$Q = \zeta - \eta = \nabla^2\eta - \eta, \tag{2.13}$$

where ∇^2 is the two-dimensional Laplacian. The initial value for the nonlinear evolution of Q follows by noting that the wave-adjustment problem has a steady limit as $t \to \infty$ and so gives the limit as $\tau \to 0$ of the advective problem. This is the two-step adjustment process referred to in §1. The scale separation assumes that vorticity advection does not produce small-scale features or, more significantly, large vorticities and strain rates, subsequently violating the quasi-geostrophic scaling. The self-consistency of the 'slow manifold' is in doubt as a general principle (Lorenz & Krishnamurthy 1987), yet here it can be verified *a posteriori*.

From (2.9),

$$Q = \operatorname{sgn} x \quad (\tau = 0). \tag{2.14}$$

The conditions required to close the η, Q problem are the values of η on the channel boundaries, constrained to be constants by (2.11). They follow by noting that only a Kelvin wave concentrated against the wall at $y = -W$ (the right-hand wall) can propagate to $x = -\infty$ and have constant values on $y = \pm W$, contributing a steady current in the final state. Hence

$$\eta \sim -1 + A_+ \mathrm{e}^{-y} \quad (1 \ll x \ll t). \tag{2.15a}$$

Similarly considering the Kelvin wave concentrated on $y = W$ (the left-hand wall) gives

$$\eta \sim 1 + A_- \mathrm{e}^{y} \quad (1 \ll -x \ll t). \tag{2.15b}$$

The undetermined amplitudes A_+, A_- of the waves are fixed by noting from (2.11) that (2.15a, b) coincide on $y = \pm W$. Thus

$$\eta \sim -1 + \operatorname{sech} W \mathrm{e}^{-y} \quad (1 \ll x \ll t), \tag{2.16a}$$

$$\eta \sim 1 - \operatorname{sech} W \mathrm{e}^{y} \quad (1 \ll -x \ll t), \tag{2.16b}$$

$$\eta = \mp \tanh W \quad (y = \pm W, \quad t \gg 1), \tag{2.17}$$

coinciding with the results of the full wave analysis in Gill (1976, 1982). There is a net flux along the channel in the positive x-direction having a y-average down-channel flow

$$U(W) = W^{-1} \tanh W, \tag{2.18}$$

which has a maximum value of unity for narrow channels and vanishes algebraically with increasing channel width. This flux is constant in time, owing to the striking ability of Kelvin waves to level the fluid at a rigid boundary. Deviations from level surfaces at boundaries are known to be important in the actual ocean, where they are associated with diffusive or strongly nonlinear effects and the presence of external stresses (Godfrey 1989). The nonlinear evolution here determines solely the redistribution of potential vorticity and fluid, while retaining the flux U. Note how ϵ has been scaled out of the problem, leaving W as the only adjustable parameter. Hence for larger ϵ, the speed of the nonlinear evolution is increased, but the resulting fields of surface height and velocity are identical to those obtained with smaller ϵ.

System (2.12)–(2.14), (2.17) gives a well-posed problem for the advective evolution of the flow, with the initial state given by the final state of the Gill problem. This wave-adjusted state follows directly by solving (2.13), (2.14), (2.17) at $\tau = 0$, to give (see Appendix)

$$Q_0(x, y) = \operatorname{sgn} x, \tag{2.19}$$

$$\eta_0(x, y) = -\sinh y \operatorname{sech} W + \operatorname{sgn} x \left\{ -1 + \cosh y \operatorname{sech} W + \frac{2}{W} \sum_{m=0}^{\infty} \frac{(-1)^m}{a_m (1 + a_m^2)} \cos(a_m y) \exp\left[-(1 + a_m^2)^{\frac{1}{2}} |x| \right] \right\}, \tag{2.20}$$

$$u_0(x, y) = \operatorname{sech} W \exp(-y \operatorname{sgn} x) + \operatorname{sgn} x \frac{2}{W} \sum_{m=0}^{\infty} \frac{(-1)^m}{(1 + a_m^2)} \sin(a_m y) \exp\left[-|x| (1 + a_m^2)^{\frac{1}{2}} \right], \tag{2.21}$$

$$v_0(x, y) = -\frac{2}{W} \sum_{m=0}^{\infty} \frac{(-1)^m}{a_m (1 + a_m^2)^{\frac{1}{2}}} \cos(a_m y) \exp\left[-|x| (1 + a_m^2)^{\frac{1}{2}} \right], \tag{2.22}$$

where $a_m = (m+\frac{1}{2})\pi/W$. By construction η_0 is continuous across $x = 0$ so the term within brackets vanishes there, giving

$$\eta_0(0,y) = -\frac{\sinh y}{\cosh W}, \quad u_0(0,y) = \frac{\cosh y}{\cosh W}. \tag{2.23}$$

Throughout the motion a particle retains its initial value of Q. Moreover, once the distribution of Q is known, the corresponding surface displacement follows by inverting (2.13) subject to the boundary conditions (2.17). Thus it is sufficient to follow the evolution of the bounding line between the two regions of differing Q, i.e. the potential vorticity front.

Following this evolution is greatly simplified by considering the flow in a frame S' with Cartesian axes $Ox'y'z'$ coincident with S at $\tau = 0$, but translating along the channel at the y-average down-channel flow speed $U(W)$, so that

$$(x', y', z') = (x - U(W)\tau, y, z). \tag{2.24}$$

Introduce Q_1, the deviation at any time τ of Q from the value obtained by simply advecting the initial value Q_0 at speed $U(W)$, i.e.

$$Q_1(x,y,\tau) = Q(x,y,\tau) - Q_0(x - U(W)\tau, y),$$

or

$$Q_1(x',y',\tau) = Q(x',y',\tau) - Q_0(x',y'). \tag{2.25}$$

The conservation of Q in S' is given by

$$Q_\tau + J'(\eta - U(W)y', Q) = 0. \tag{2.26}$$

Typical regions involved are sketched in figure 2. Figure 2(*a*) shows the advected, unaltered initial Q_0 with the dividing line C_0 between differing values given by $x = U(W)\tau$. Figure 2(*b*) gives a hypothetical value of Q at time τ with C_1 as the separatrix. Figure 2(*c*) illustrates the difference $Q_1 = Q - Q_0$, non-zero solely in the shaded regions, where it equals ± 2. Since there is no net flux across the moving line C_0, the areas of positive and negative Q_1 are equal. The total signed area of Q_1 vanishes. This furnishes a check on the global accuracy of the numerical methods discussed later. The division of the problem into Q_0 and Q_1 parts is in no way a perturbation expansion, but rather is aimed at maximal computational efficiency.

Now consider the surface elevation corresponding to Q_1. Analogously to (2.24), introduce

$$\eta_1(x,y,\tau) = \eta(x,y,\tau) - \eta_0(x - U(W)\tau, y),$$

so

$$\eta_1(x',y',\tau) = \eta(x',y',\tau) - \eta_0(x',y'). \tag{2.27}$$

Then (2.13), (2.14), (2.17) become

$$Q_1 = \nabla^2\eta_1 - \eta_1, \tag{2.28}$$

$$\eta_1 = 0 \quad (y = \pm W, \quad \tau > 0), \tag{2.29}$$

$$Q_1 = 0 \quad (\tau = 0). \tag{2.30}$$

Note how advecting the initial field of Q_0, η_0 (and corresponding u_0, v_0) effectively shifts the Gill solution to a more efficient location, where the deviations from it (Q_1, η_1, u_1, v_1) will be smallest. This is a matter of convenience rather than necessity.

Here and in the remainder of this section it is no longer necessary to distinguish between the dashed and undashed frames as (2.28), (2.29) are independent of τ. The compact support of Q_1 means that this system is ideally suited for computation by contour dynamics. At a given instant (2.28) is inverted using the homogeneous

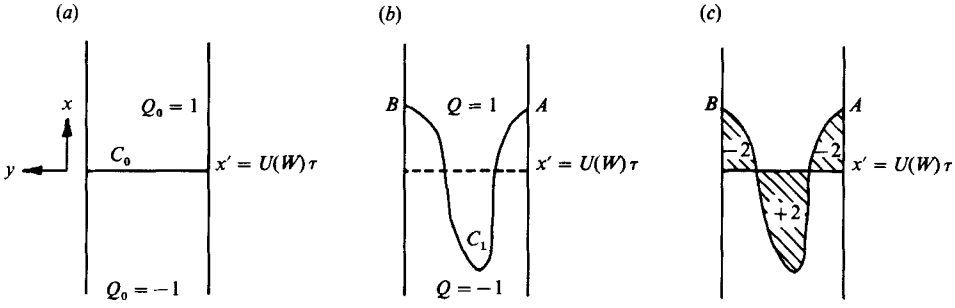

FIGURE 2. The various potential vorticity distributions. (*a*) The advected unaltered initial distribution Q_0 with values separated by the straight line C_0 at $x = U(W)\tau$. (*b*) A hypothetical distribution Q at a later time $\tau > 0$. The separatrix is the curved line C_1 joining A and B. (*c*) The difference $Q_1 = Q - Q_0$, non-zero in the shaded regions alone where it takes the values ± 2.

boundary conditions (2.29) to give η_1, hence η and the velocities at any point in the channel. In particular the velocities of particles on the line separating the two values of Q are known. Thus the position of this line can be advanced with time, a new field of Q_1 obtained and so on.

It remains to discuss the inversion of (2.28), (2.29). Let $G(x, y, \xi, \mu)$ be the Green function for (2.28), (2.29) so G satisfies

$$\nabla^2 G - G = \delta(\xi)\,\delta(\mu), \tag{2.31}$$

$$G = 0 \quad (y = \pm W). \tag{2.32}$$

Then
$$\eta_1(x, y) = \int Q_1(\xi, \mu)\, G(x, y, \xi, \mu)\, \mathrm{d}\xi\, \mathrm{d}\mu. \tag{2.33}$$

Taking the gradient of (2.33) and using Green's theorem in the plane gives the velocity components in terms of a single path integral, i.e.

$$(u_1, v_1)(x, y) = 2 \oint_{\partial Q_1} G(x, y, \xi, \mu)\, (\mathrm{d}\xi, \mathrm{d}\mu), \tag{2.34}$$

provided the boundary of Q_1 is described so that low values of Q_1 lie to the right. Particle velocities in the frame S' are then given by

$$(u, v) = (u_0 + u_1 - U(W), v_0 + v_1). \tag{2.35}$$

A number of forms can be found for G. Direct solution of (2.31), (2.32) by Fourier integral gives

$$G(x, y, \xi, \mu) = -\frac{2}{\pi} \int_0^\infty \begin{Bmatrix} \sinh K(y+W) \sinh K(w-\mu) \\ \sinh K(\mu+W) \sinh K(W-y) \end{Bmatrix} \frac{\cos k(x-\xi)\, \mathrm{d}k}{K \sinh 2KW}, \quad \begin{cases} -W < y < \mu, \\ \mu < y < W, \end{cases} \tag{2.36}$$

where $K^2 = k^2 + 1$. Although valid for all W this form is cumbersome for computation and an equivalent expression can be derived by considering images of a free-surface point vortex. This gives

$$G(x, y, \xi, \mu) = \frac{1}{2\pi} \sum_{n=-\infty}^{\infty} K_0\{[(x-\xi)^2 + (y-\mu+4nW)^2]^{\frac{1}{2}}\} - K_0\{[(x-\xi)^2 + (y+\mu+2W+4nW)^2]^{\frac{1}{2}}\}. \tag{2.37}$$

Series (2.37) converges exponentially for all non-zero W, converging most rapidly for

wide channels and least rapidly for narrow channels. For extremely narrow channels, $W \ll 1$, free-surface deformation is unimportant, (2.31) reduces to the standard Laplacian, and G gives the field associated with a point charge between grounded plates, having the simple form

$$G(x, y, \xi, \mu) = \log|\tanh\{[(x-\xi)+\mathrm{i}(y-\mu)]/W\}| + O(W). \tag{2.38}$$

The exponential behaviour of the Green function makes the free-surface problem far more local than the logarithmic tail of point vortices in a two-dimensional fluid.

The integral (2.34) was computed for each of 1000 points around the contour at each timestep ($\Delta\tau = 0.25$ for wide channels and 0.05 for narrower channels) using the CRAY X-MP. Seven terms in the series (2.37) ($n = -3$ to $n = 3$) were sufficient to evaluate G for all channel widths. The Gill solution velocities u_0, v_0 were evaluated with the first ten terms of the series (2.21), (2.22). After computation of u_0, v_0, u_1, v_1 the points were advanced using a fourth-order Runge-Kutta scheme. Points were respaced evenly along the contour line separating regions of non-zero and zero Q_1 after each timestep, to prevent the development of sparse regions with few points. Spline interpolation was utilized in this procedure for cases with $2W > 1$, and linear interpolation for $2W \leqslant 1$ (where contours approached the walls too closely for spline interpolation to be useful). Integrals for the contour segments adjacent to the point whose velocity was being computed (which contain a singularity), and integrals for contour segments adjacent to walls (where the slope of the contour changes suddenly) were computed using appropriate analytical expressions. Elsewhere the integral for each contour segment was approximated using the Euler method (as in Zabusky *et al.* 1979).

Global error was calculated as the deviation of the total signed error of Q_1 from zero, normalized by $4W^2$ (the width of the channel squared). Values of global error ranged from 2.2×10^{-4} to 2.8×10^{-2} at the end of each run, the largest value occurring for the longest run ($\tau = 75$) of the channel of width $2W = 10$.

3. Results

Since W, the channel half-width in Rossby radii, is the only free parameter in the scaled nonlinear problem, it is sufficient to consider a range of channel widths to completely characterize the slow nonlinear evolution. Here we consider channel widths in the range 0.2–25.0.

3.1. *Wide channels* ($2W = 25$, $2W = 10$)

For $W \gg 1$ frames S and S' coincide for times $\tau \ll W$. The two walls are independent and apart from Rossby radius-wide boundary layers near $x = 0$, η is unaltered, i.e.

$$\eta_0 \sim -1 + 2\mathrm{e}^{-(y+W)} \quad (x \gg 1), \tag{3.1a}$$

$$\eta_0 \sim -1 - 2e^{(y-W)} \quad (-x \gg 1), \tag{3.1b}$$

$$\eta_0 \sim -1 + \mathrm{e}^{-x} \quad (x > 0 \quad \{|y| - W\} \gg 1), \tag{3.2a}$$

$$\eta_0 \sim 1 - \mathrm{e}^{x} \quad (x < 0 \quad \{|y| - W\} \gg 1). \tag{3.2b}$$

The cross-channel integral of down-channel flux has the asymptotic value of 2. Figure 3 gives initial contours of surface elevation η_0, and so streamlines, for $2W = 25$. Fluid drains from the region of high surface elevation in a narrow current against the wall at $y = W$, crosses the channel in a current straddling $x = 0$ and con-

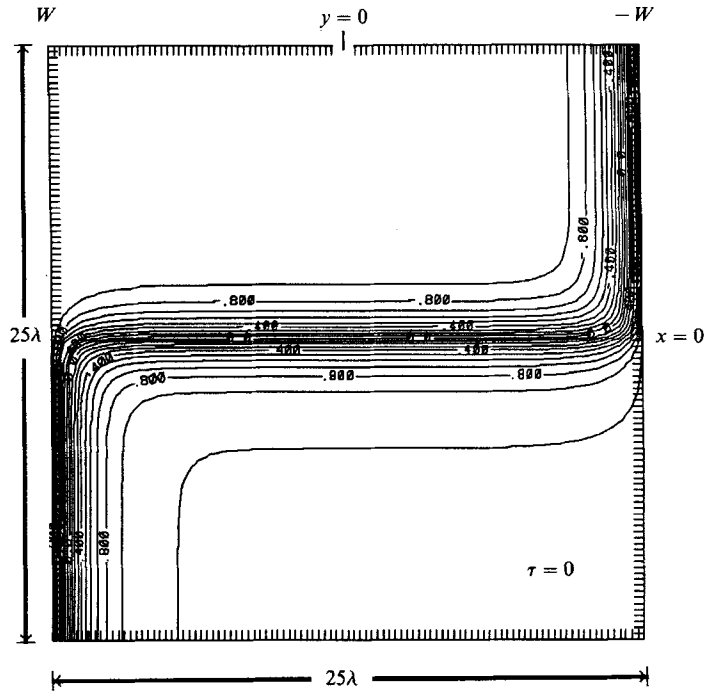

FIGURE 3. Contours of the wave-adjusted free-surface elevation η_0 from (2.20) for $2W = 25$, a channel of width 25 Rossby radii. Fluid drains from the region of high surface elevation in a narrow current against the wall at $y = W$, crosses the channel in a current straddling $x = 0$, and continues into the low region along the wall at $y = -W$. These contours give streamlines of the flow before the further advective adjustment.

tinues into the low region along the wall at $y = -W$. The velocity is perpendicular to the gradient of potential vorticity everywhere except in the two small turning regions where the cross-stream flow leaves and returns to the walls, i.e. $x \sim O(1)$, $\{|y| - W\} \sim O(1)$. Initially it is in these regions alone that further advective adjustments take place. The direction of the first deviation of the front of Q is given by the wave adjusted velocity $u_0(0, y)$ from (2.23), although rapidly, by times $\tau - W^{-1} \ll 1$, the advection of relative vorticity will become equally important. Such initial deviations are confined to narrow boundary layers against each wall. The adjustments in the two regions are independent at this stage, and between them they give the prototypes required to discuss all possible adjustments of narrow currents abutting isolated walls.

By the time $\tau \sim 5$, nonlinear evolution of the vorticity front has produced a thin wedge of lower potential vorticity fluid (henceforth termed 'new fluid') on the right-hand wall, and a Gaussian-shaped nose of that fluid on the left-hand wall (figure 4). The cross-channel thickness of the right-hand wedge varies uniformly, and is less than one Rossby radius wide ($\Delta y < 1$) over much of its length. The left-hand nose is considerably thicker over its length. In the vicinity of the initial discontinuity, the intrusion of new fluid is greater than one Rossby radius wide on both sides of the channel. Both the wedge and the nose lengthen with time in the down-channel direction; as a result, the boundary between the fluids aligns nearly parallel to the wall on the right-hand side. The left-hand nose lengthens in a fashion which appears to preserve its shape near the head. At the head itself, the boundary lies nearly perpendicular to the left-hand wall (angle of $\sim \frac{1}{3}\pi$ at $\tau = 5$).

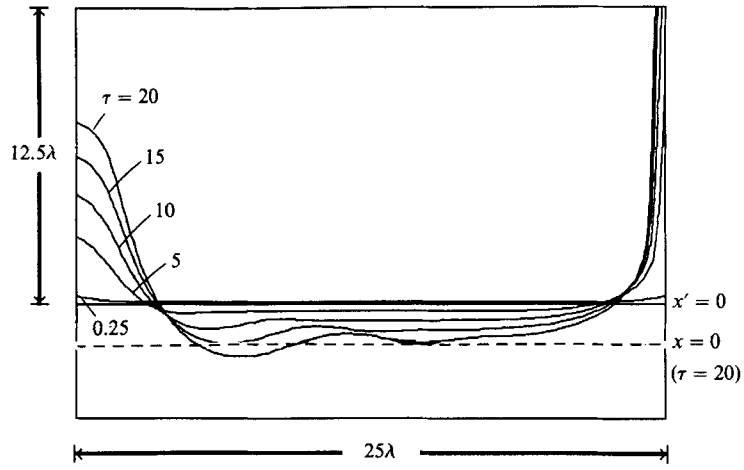

FIGURE 4. Evolution of the potential vorticity front in a channel of width $2W = 25$, for times $\tau = 0.25, 5, 10, 15, 20$. The front is plotted in the moving frame S', which translates downstream at a rate of $U = 0.08$. A dashed line indicates the position of the initial height discontinuity ($x = 0$) relative to the front at $\tau = 20$.

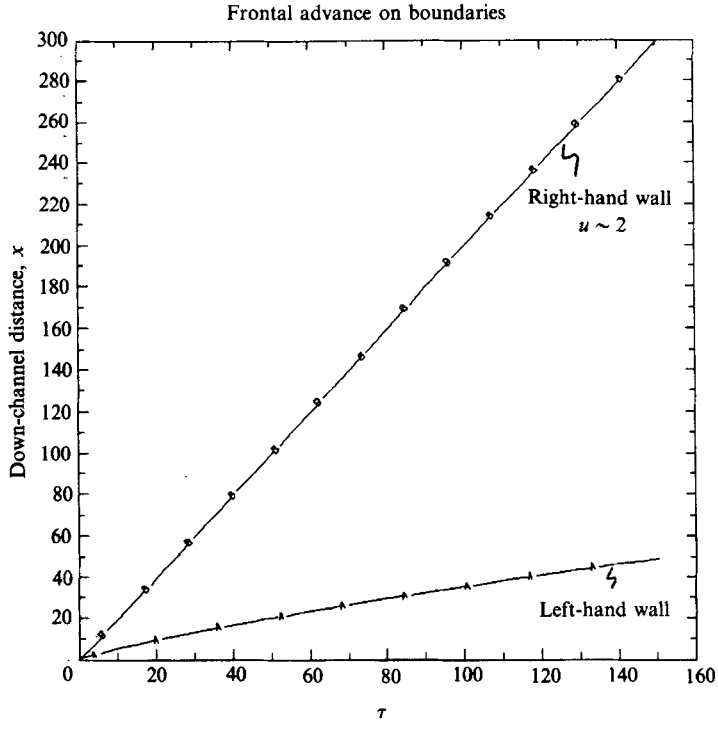

FIGURE 5. Progression of the potential vorticity front along left- and right-hand walls in the channel of width $2W = 25$.

The leading tip of the right-hand wedge of new fluid moves at a rate nearly identical with the velocity of the Gill solutions for the linear problem – that is, at a rate of 2 (figure 5). The left-hand nose advances at the considerably slower rate of ~ 0.25. As both sides progress, deformation of the interior front penetrates further inward from the left-hand wall. By $\tau \sim 20$, the influence of the left-hand wall

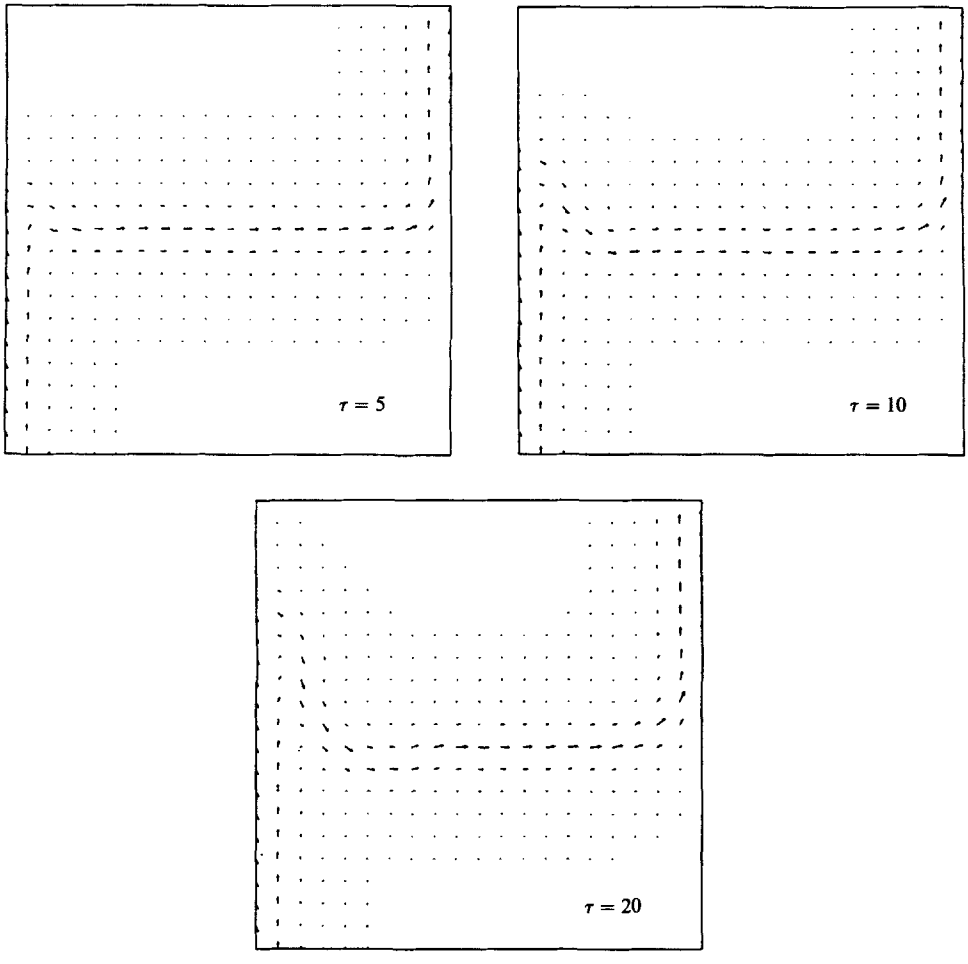

FIGURE 6. Evolution of the velocity field in a channel of width $2W = 25$ for times $\tau = 5$, 10, 20. Velocity vectors are plotted in the moving frame S', as in figure 4.

is evident all the way out to the centre of the channel. At this point the moving coordinate frame S' has advanced a distance of $\Delta x = 1.6$ relative to the origin, but an interior section of the fluid front has not yet moved downstream from its initial location.

Velocity vectors for this sequence of frames exhibit how the boundary flow on the left-hand wall has crept over the initial step location with the nose of new fluid, doubling back at an increasingly distant location to rejoin with the linearly adjusted interior flow (figure 6). The effect of the wedge of new fluid on the right-hand wall is not so obvious in this figure. However, a cross-channel profile of down-channel velocity at $x = 0$ (figure 7) clearly shows how the penetration of new fluid sharply reverses the sign of relative vorticity in the vicinity of the right-hand wall, from its linearly adjusted positive value to a new, negative value. As a natural result of the sign-change in relative vorticity, the jet of highest velocity appears everywhere to lie on the boundary between old and new fluid.

The conservation of potential vorticity following fluid columns readily explains these results. Initial linear adjustment stretched fluid columns on the right-hand wall

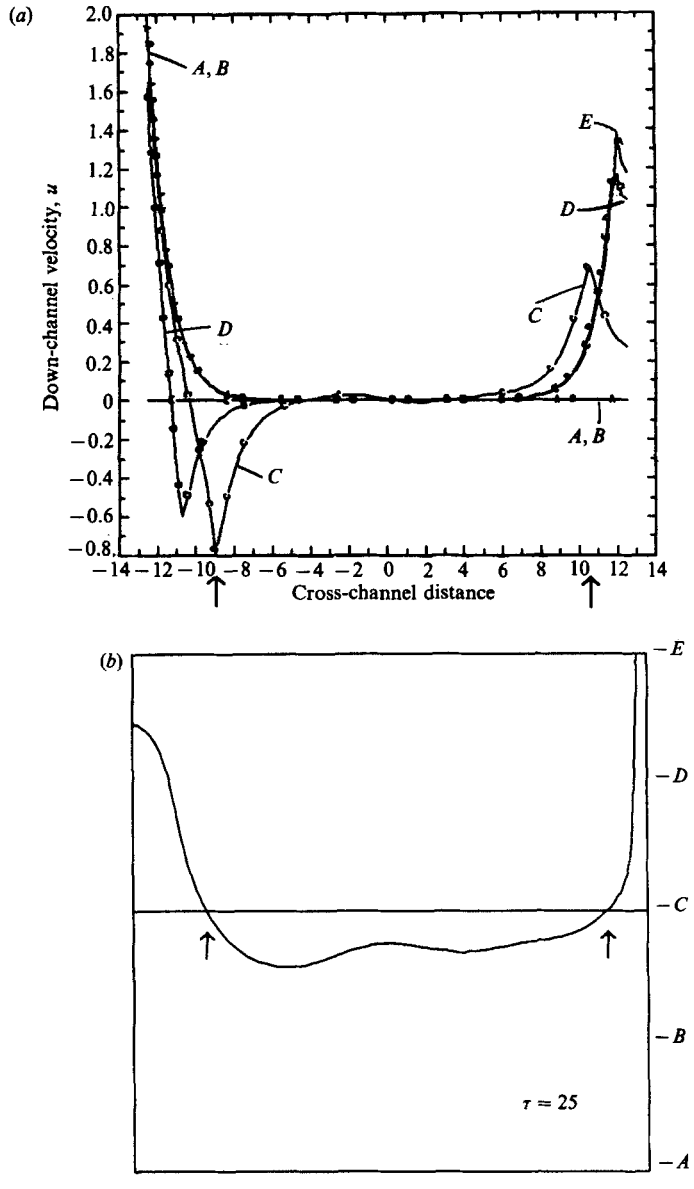

FIGURE 7. (*a*) Cross-channel profiles of downstream velocity $u(x', y')$ at $\tau = 25$ for the several locations along the channel of width $2W = 25$ ($x' = 0, \pm 6.25, \pm 12.5$) marked in (*b*). The position of the potential vorticity front at $\tau = 25$ is shown for comparison.

everywhere downstream from the origin, producing a velocity profile with positive relative vorticity. Once the new fluid enters this downstream, right-hand region, it must acquire negative relative vorticity to the extent that all fluid columns of this new fluid are compressed from their initial height. Hence the vorticity advection shifts the velocity maximum away from the right-hand wall, towards the left-hand side of the channel.

The surface-height field corresponding to the velocity field at $\tau = 20$ (figure 8) exhibits especially the intrusion of new fluid on the left-hand wall, and the deformation of the interior pattern between that wall and the centre of the channel.

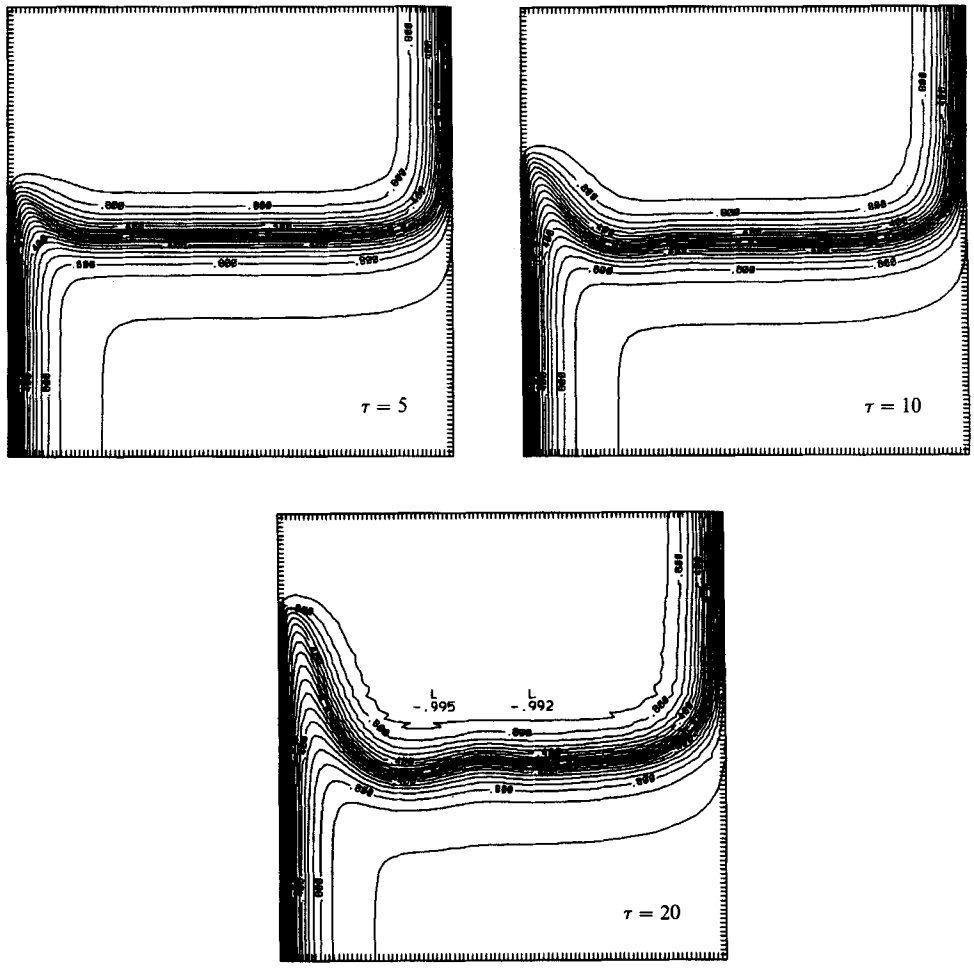

FIGURE 8. Evolution of the surface-height field in a channel of width $2W = 25$ for times $\tau = 5$, 10, 20. Height contours are plotted in the moving frame S', as in figures 4 and 6. Numerical jitter results from aliasing effect of points used to represent the potential vorticity front as they sweep through the grid of points used to construct the height field.

One is naturally drawn to ask whether the information from either wall will ultimately affect the dynamics all across the channel, i.e. whether the two walls will 'communicate' with each other, and what the ultimate velocity and surface-height fields must be. Simulations beyond $\tau = 20$ are of course necessary to address this issue. An extended run of the model with $2W = 25$ is problematical, insofar as the (evenly respaced) points around the contour become widely separated given sufficient time, an effect which can be overcome only at considerable computational cost. However, an extended run with a slightly narrower channel, $2W = 10$, clearly illustrates downstream translation of the fluid front from its original location at $x = 0$ everywhere across the channel by $\tau = 25$ (figure 9*a*) The time required for such cross-channel communication to prevail appears to be a monotonically increasing function of channel width, as described in §4.3. By $\tau \sim 50$, the fluid front is everywhere displaced further than one Rossby radius downstream from its initial location. A compressed view of the front reveals the persistence of the noselike

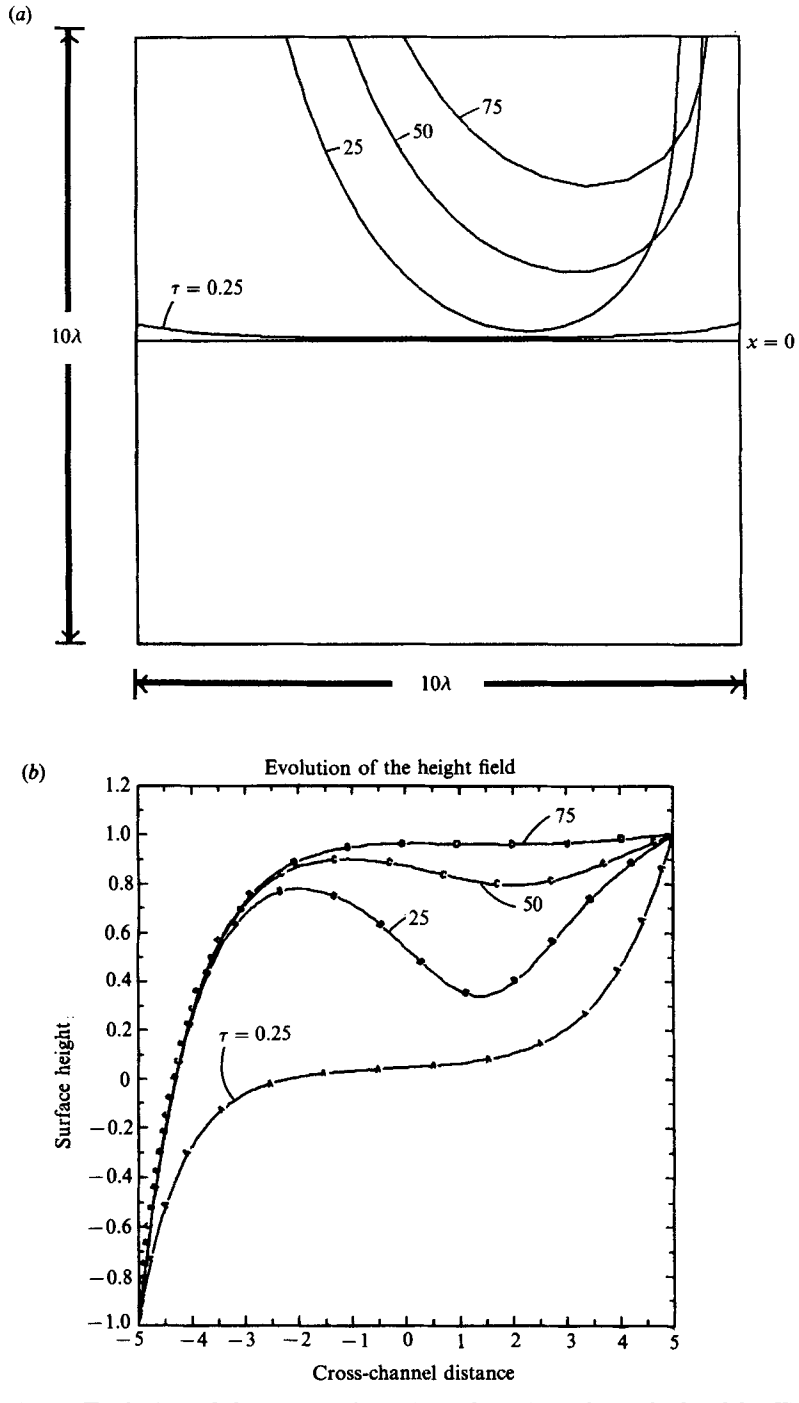

FIGURE 9. (*a*) Evolution of the potential vorticity front in a channel of width $2W = 10$ for times $\tau = 0.25, 25, 50, 75$. Position of the front is plotted in the fixed frame S', illustrating the complete detachment of the front from the position of the initial height discontinuity. (*b*) Corresponding cross-channel sections of free-surface height $\eta(x, y)$ *for* $x = 0$, illustrating the evolution from the antisymmetric profile at $\tau \sim 0$ to the upstream height profile by $\tau = 75$.

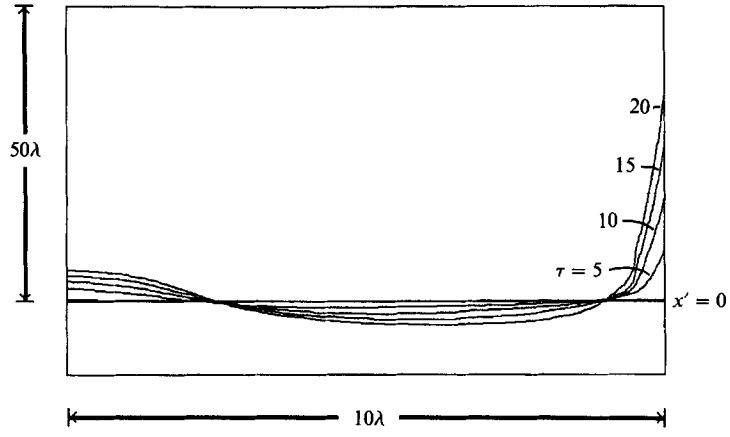

FIGURE 10. Evolution of the potential vorticity front in a channel of width $2W = 10$ for times $\tau = 5$, 10, 15, 20. The front is plotted in the moving frame S', and the x'-axis is compressed to illustrate the down-channel structure of the front.

intrusion on the left-hand wall and the wedgelike intrusion on the right for times up to $\tau = 20$ (figure 10).

Evolution towards the final shape of the surface-height field is best illustrated by a time series of height cross-sections for the $2W = 10$ channel (figure 9*b*). Consider the initial location of the height discontinuity ($x = 0$). At $\tau = 0$ (linearly adjusted state) the surface height has an antisymmetric form. The height near both walls increases dramatically with the intrusion of new fluid, though nowhere does it exceed the constant value on the right-hand wall. Eventually the height rises to the level of the right-hand wall all across the channel, except for the boundary region against the left-hand wall. By $\tau \sim 75$, the cross-section has in fact assumed nearly the same profile as was present far upstream of the initial height discontinuity; fluid has everywhere 'washed downstream' beyond $x = 0$ in the channel. Apparently, for sufficiently large τ, there is a value of x beyond which all new fluid has washed downstream, leaving the left-hand jet as the final state.

3.2. *Intermediate width channel* ($2W = 5$)

The nonlinear evolution of a channel only 5 Rossby radii wide proceeds differently from the wide channel cases. Initially the evolution is similar; a wedge of new fluid penetrates on the right-hand wall, and a nose of new fluid penetrates on the left-hand wall. However, the two walls rapidly communicate with each other and a new pattern emerges. By $\tau \sim 5$ the linear interior solution holds nowhere across the channel, and fluid has everywhere washed downstream a distance of at least one Rossby radius (figure 11*a*). By $\tau \sim 10$ a new effect appears; the right-hand wedge has begun to pinch off from the main body of the new fluid (figure 11*b*). The front of new fluid on the right-hand wall initially moves along that wall at a rate close to the wave-adjusted boundary current speed ($u \sim 2$, as in the wide channel case), whereas the front on the left-hand wall moves faster than for the wide channel case, initially at a rate of ~ 0.5 (figure 12*a*). This faster rate cannot be attributed simply to penetration of the Gill solution from the right-hand wall. For $x \gg 0$, the Gill solution at $y = -W$ is only $u = 0.013$ for this intermediate width channel. Hence, nonlinear effects (e.g. faster self-advection of the nose, due to closer proximity of its image) must be responsible for the difference. By $\tau \sim 20$ the rate of advance has slowed

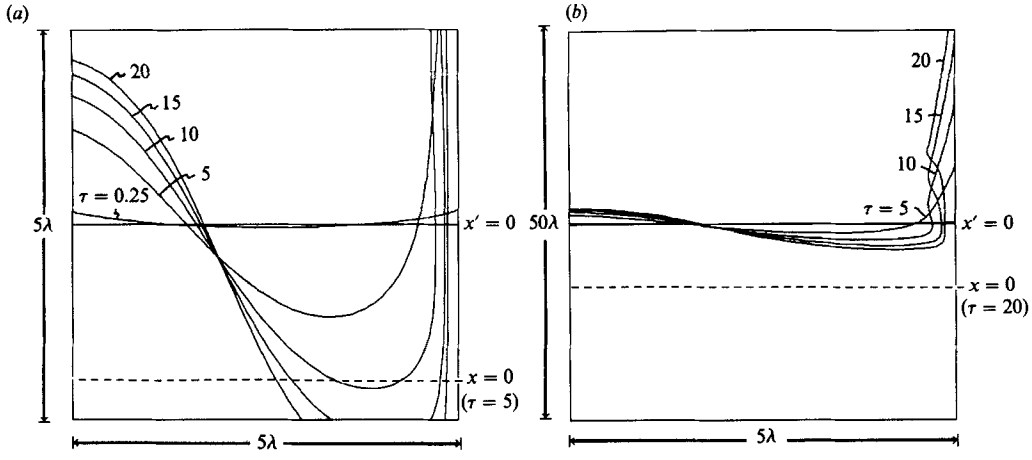

FIGURE 11. (*a*) Evolution of the potential vorticity front in a channel of width $2W = 5$ for times $\tau = 0.25, 5, 10, 15, 20$. The front is plotted in the moving coordinate system S', which translates downstream at a rate $U = 0.4$. A dashed line indicates the position of $x = 0$ at $\tau = 5$; the position $x = 0$ is outside the domain of the figure for subsequent times. (*b*) The x'-axis is compressed to illustrate the pinching-off of fluid on the right-hand wall. A dashed line indicates the position of $x = 0$ at $\tau = 20$.

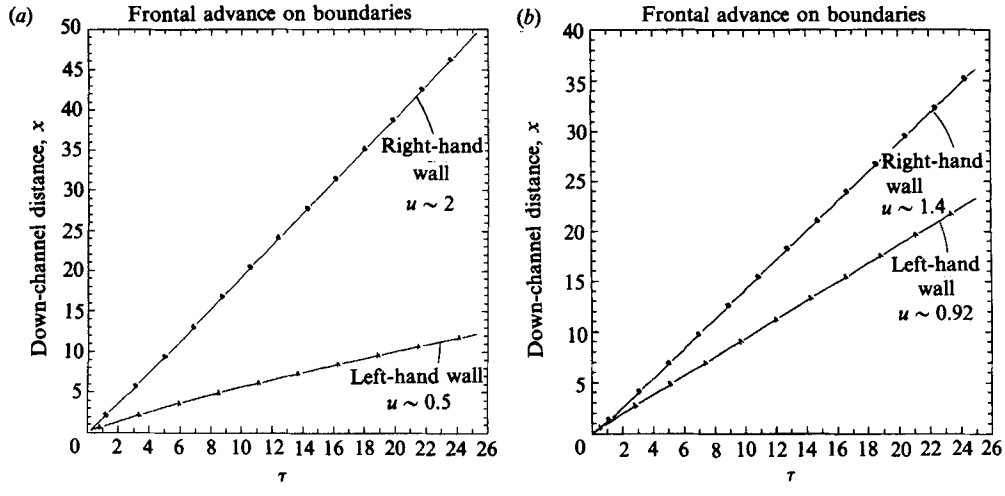

FIGURE 12. Progression of the potential vorticity front along left- and right-hand walls for: (*a*) the channel of width $2W = 5$; (*b*) the channel of width $2W = 1$.

appreciably, approaching that of the mean down-channel flow speed U (~ 0.4); hence the left-hand portion of the contour approaches a steady form in the moving frame S'.

3.3. *Narrow channel* ($2W = 1$)

For a channel which is only one Rossby radius wide, the communication between walls is especially rapid, and the fluid front has shifted downstream across the entire channel by $\tau \sim 2$ (figure 13*a*). On the right-hand wall, the wedge of new fluid pinches off and moves ahead, as a coherent feature, from the rest of the new fluid mass. The left-hand intrusion no longer has a noselike shape as in the wider channels, but rather assumes a linear shape which joins with the central portion of the fluid front. Indeed, by $\tau = 8$ there results a straight front, tilted at 0.24 radians with respect to the cross-

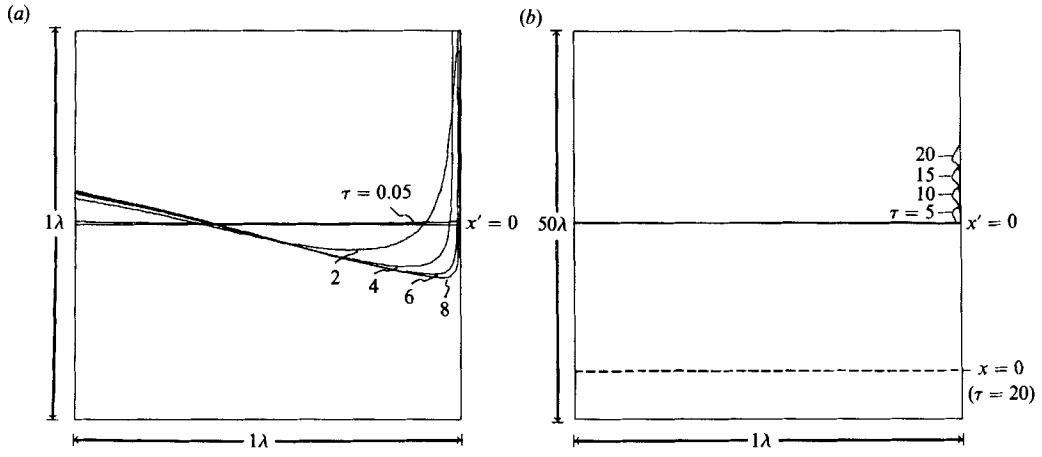

FIGURE 13. (*a*) Evolution of the potential vorticity front in a channel of width $2W = 1$ for times $\tau = 0.05, 2, 4, 6, 8$. The front is plotted in the moving frame S', which translates downstream at a rate $U = 0.93$. The position $x = 0$ lies outside of the domain of this figure for $\tau = 2$ and subsequent times. (*b*) The x'-axis is compressed to illustrate the pinching-off of fluid on the right-hand wall, and its subsequent travel ahead of the remaining potential vorticity front. A dashed line indicates the position of $x = 0$ at $\tau = 20$.

channel axis, which moves down-channel at nearly the speed of the translating coordinate system $S'(U \sim 0.93$ in this case). A compressed view of the front (figure 13*b*) illustrates the coherent structure of pinched-off fluid on the right-hand boundary, which moves ahead of the straight cross-channel front at a rate of 0.48 in S' (in the 'fixed' frame S this is $u = 1.4$; see figure 12*b*). The coherent structure is nearly fore–aft symmetric; asymmetry is due to the long, thin tail connecting this part of the fluid front to the linear cross-channel section.

Velocity vectors drawn in the fixed coordinate system S for a region far downstream from the initial discontinuity ($x = 9.5$ to 10.5) illustrate the reversal in relative vorticity which occurs all across the channel once the new fluid has washed completely past the channel interior (figure 14). As with the wider channels, the down-channel profile of height and velocity is ultimately replaced by the upstream condition, as the new fluid is washed downstream.

Certain features of the narrow channel case do not conform to a Rossby radius scale. In particular, the coherent structure of new fluid on the right-hand wall is only $\sim 5\,\%$ of the Rossby radius in width. However, the characteristic alongshore length of this feature is close to the Rossby radius scale, being in the range $\Delta x \sim 1$–2. After the transients have carried downstream, the final state of flow establishes the Rossby radius as the dominant width scale, yet with the velocity maximum having moved from the right-hand wall to the left.

3.4. *Very narrow channel* ($2W = 0.2$)

At this very narrow limit, the mean translation speed U closely approximates its asymptotic value of 1. The majority of the surface height contrast has been cancelled by waves of almost constant cross-stream properties and equal and opposite amplitudes travelling upstream and downstream. While the Gill solution for down-channel flow is nearly constant across the channel, a wedge of new fluid still manages to surge ahead of the mean flow and pinch off into a coherent structure (figure 15). A compressed view of the coherent feature reveals a blunt nose at its head (resolved

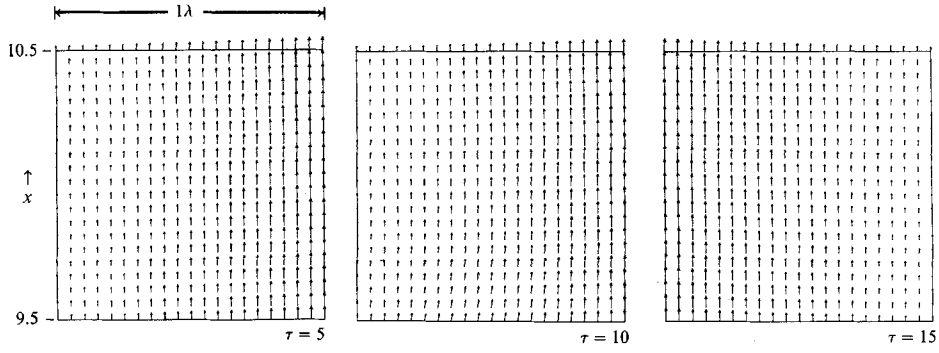

FIGURE 14. Velocity field between $x = 9.5$ and 10.5 in the narrow channel (fixed coordinate system S) for $\tau = 5$, 10, 15. The potential vorticity front passes through at $\tau \sim 10$, reversing the sign of relative vorticity across the channel.

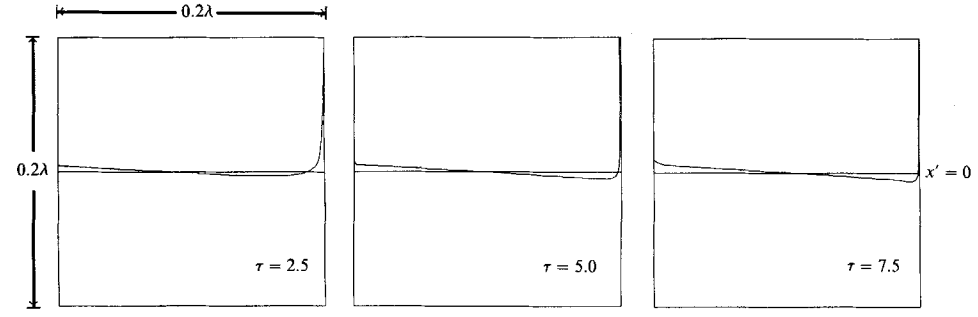

FIGURE 15. Evolution of the potential vorticity front in a channel of width $2W = 0.2$ for times $\tau = 2.5$, 5.0, 7.5. The front is plotted in the moving frame S', which translates downstream at a rate $U = 0.99$.

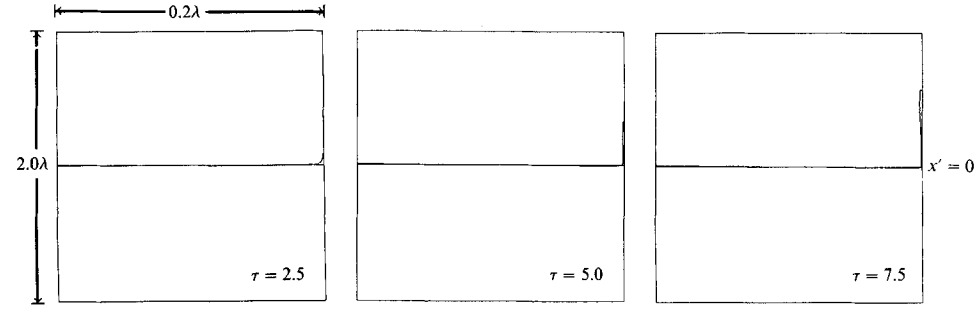

FIGURE 16. Evolution of the potential vorticity front for a channel of width $2W = 0.2$ as in figure 15, but with the x'-axis compressed to illustrate the pinching-off and propagation of a blunt-nosed coherent feature.

with 9 points at $\tau = 7.5$ in our simulation), as compared to the sharp wedge of the wider channel cases compare figures 16 and 13). Again note the cross-channel scale of this feature is considerably smaller (by a factor of 0.005) than one Rossby radius.

As with the case $2W = 1$, the main cross-channel section of the fluid front is a nearly straight line, rotated in a negative sense with respect to the cross channel axis (0.070 radians by $\tau = 7.5$). This section translates downstream at a rate $U \sim 0.99$.

4. Discussion

4.1. *Evolution of wedges of uniform potential vorticity fluid*

A more thorough understanding of the wide channel evolution results from analytically examining the near-boundary behaviour of isolated wedges of fluid. Such wedges serve as idealizations of the frontal behaviour at left- and right-hand walls in the wide channel before cross-channel communication is complete. Consider the isolated wedge of uniform potential vorticity fluid and its image shown in figure 17. The induced velocity at a point which lies on the fluid front at a distance r from the wall can be expressed as:

$$\left.\begin{matrix} u \\ v \end{matrix}\right\} = \left\{\begin{matrix} \cos\theta \\ -\sin\theta \end{matrix}\right\} \frac{-\Delta Q}{2\pi}\left(\int_0^\infty K_0(z)\,\mathrm{d}z + \int_0^r K_0(z)\,\mathrm{d}z\right)$$
$$+\left\{\begin{matrix} \cos\theta \\ \sin\theta \end{matrix}\right\} \frac{-\Delta Q}{2\pi}\left(\int_0^\infty K_0[(b^2+z^2)^{\frac{1}{2}}]\,\mathrm{d}z + \int_0^s K_0[(b^2+z^2)^{\frac{1}{2}}]\,\mathrm{d}z\right)$$
$$+\left\{\begin{matrix} -2 \\ 0 \end{matrix}\right\} \frac{-\Delta Q}{2\pi}\left(\int_0^\infty K_0[(a^2+z^2)^{\frac{1}{2}}]\,\mathrm{d}z + \int_0^q K_0[(a^2+z^2)^{\frac{1}{2}}]\,\mathrm{d}z\right), \tag{4.1}$$

where u, v are the velocities parallel and normal to the wall, ΔQ is the difference between the potential vorticity inside the wedge and that of the ambient fluid, θ is the angle at which the front intersects the wall, and q, r, s are as shown in the figure. Note how the region of higher potential vorticity is on the right for the path used to evaluate the contour integral.

Ideally we seek a closed form expression for each of these integrals. For the definite integrals we may use:

$$\int_0^\infty K_0[(\alpha^2+\beta^2)^{\frac{1}{2}}]\,\mathrm{d}\beta = \tfrac{1}{2}\pi \mathrm{e}^{-|\alpha|}. \tag{4.2}$$

However, there is no simple closed form available (to our knowledge) for the corresponding indefinite integrals with r, s, q as limits. Here we must appeal to the limit of small r, noting that

$$K_0(r) \to -\ln r \quad \text{as } r \to 0. \tag{4.3}$$

The utility of this approximation lies in the fact that

$$\int_0^r \ln[(a^2+b^2)^{\frac{1}{2}}]\,\mathrm{d}b = \tfrac{1}{2}[r\ln(r^2+a^2) - 2r + 2a\arctan(r/a)]. \tag{4.4}$$

In the limit of $r = 0$ (the tip of the wedge), we have the exact expression:

$$u = -\tfrac{1}{2}\Delta Q(\cos\theta - 1), \quad v = 0. \tag{4.5}$$

For the case of the right-hand wedge in the channel, $\Delta Q = -2$, and so the corresponding expression for an isolated wedge is

$$u = \cos\theta - 1. \tag{4.6}$$

Behaviour of a left-hand wedge is identical to that of a right-hand wedge with the sign of ΔQ reversed:

$$u = 1 - \cos\theta. \tag{4.7}$$

Hence for small but non-zero θ, the right-hand wedge will, with its image, tend to propagate in the up-channel direction. To this tendency must be added the underlying velocity of the Gill solution (which is the structural feature distinguishing the present problem from other researches of wall jets studied with contour

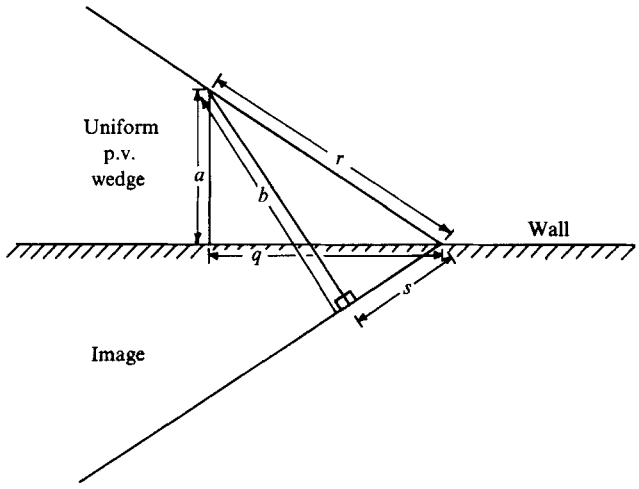

FIGURE 17. Parameters for an idealized wedge of constant potential vorticity in contact with a right-hand wall, and its image.

dynamics, e.g. Stern 1986). The net result, figure 5, is that the thin right-hand wedge of fluid moves at just under the velocity of the Gill solution, which is $u = 2$. Conversely the left-hand wedge will self-propagate in the down-channel direction, initially at maximal speed, for there $\theta = \frac{1}{2}\pi$. It can further be shown, using (4.1), (4.2) with the approximation of (4.3), (4.4), that for small but non-zero r/a on a right-hand wedge with $\Delta Q < 0$,

$$\frac{\partial u}{\partial r} < 0, \quad \frac{\partial v}{\partial r} < 0.$$

Conversely, for a left-hand wedge:

$$\frac{\partial u}{\partial r} > 0, \quad \frac{\partial v}{\partial r} > 0.$$

These results clearly imply that a right-hand wedge with $\Delta Q < 0$ will tend to rarefy, whereas the corresponding left-hand wedge will steepen. This is precisely the result observed in the evolution of the narrow wedge and broad nose in the wide channel run, despite the background shear of the Gill solution. The tendencies may be verified qualitatively by sketching the velocity vectors at a point on the wedge, owing to the closest image nodes. These will tend to rarefy or steepen according to the rule above. A further check on the analytical result is provided by a numerical run of the corresponding wedges, with the Gill velocity removed. The respective rarefaction and steepening are both evident in figure 18.

4.2. *Application of the long-wave equation*

Stern (1985) showed how the behaviour of potential vorticity fronts can sometimes be inferred using the long-wave equation:

$$\frac{\partial L}{\partial \tau} + c(L)\frac{\partial L}{\partial x} = 0, \tag{4.8}$$

where L is the y-coordinate (the distance from the boundary) of the point of interest

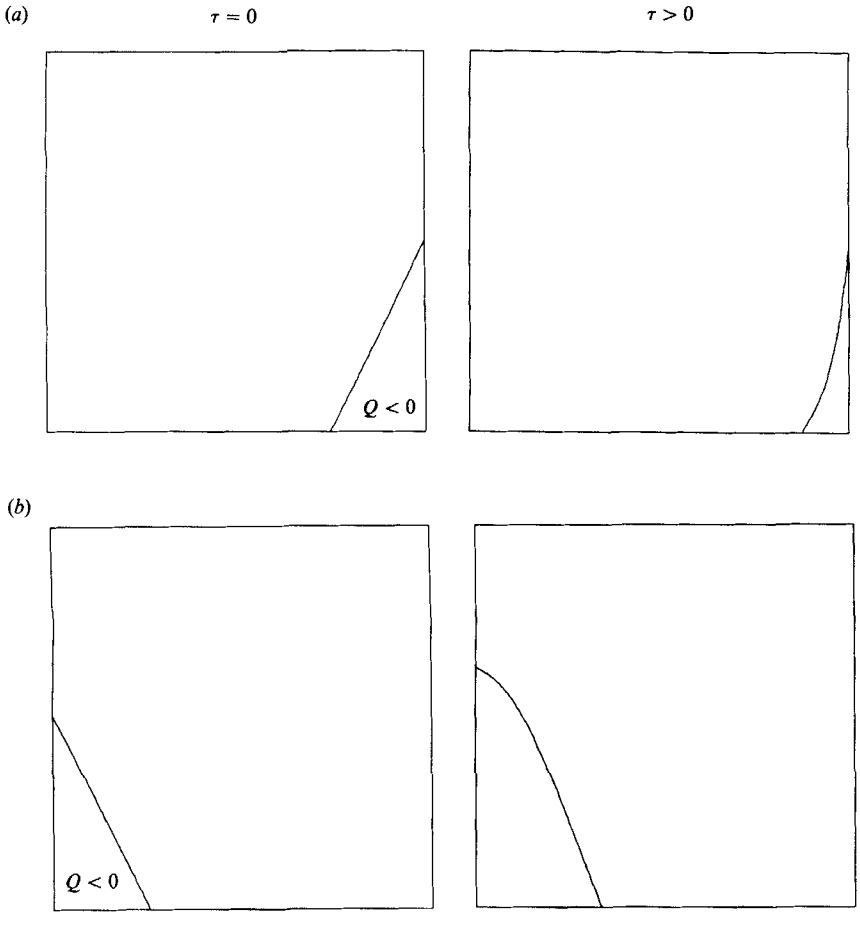

FIGURE 18. Evolution of isolated wedges of negative potential vorticity against: (*a*) right-hand and (*b*) left-hand walls. Rarefaction and steepening are observed in the respective cases.

on a potential vorticity front. First, note that if $L(x,t)$ is slowly varying in x, we can approximate v for the front using

$$v = \frac{\mathrm{d}L}{\mathrm{d}\tau} \cong \frac{\partial L}{\partial \tau} + u\frac{\partial L}{\partial x}. \tag{4.9}$$

This becomes the long-wave equation if we can make the substitution

$$c(L) \equiv u - \frac{v}{\partial L/\partial x}. \tag{4.10}$$

Stern (1986) showed that for a front at a distance $L(x,t)$ from the boundary, the induced velocities are:

$$u = -\tfrac{1}{2}\Delta Q(1 + \mathrm{e}^{-2L} - 2\mathrm{e}^{-L}), \tag{4.11}$$

$$v = -\tfrac{1}{2}\Delta Q\frac{\partial L}{\partial x}(1 - \mathrm{e}^{-2L}), \tag{4.12}$$

whence

$$c(L) = +\Delta Q(\mathrm{e}^{-L} - \mathrm{e}^{-2L}). \tag{4.13}$$

Now, for the case of a channel, where all images must be considered, the corresponding expressions are

$$u = -\tfrac{1}{2}\Delta Q \sum_{n=-\infty}^{\infty} (e^{-|4nW|} + e^{-|4nW+2L|} - 2e^{-|4nW+L|}), \tag{4.14}$$

$$v = -\tfrac{1}{2}\Delta Q \frac{\partial L}{\partial x} \sum_{n=-\infty}^{\infty} (e^{-|4nW|} - e^{-|4nW+2L|}), \tag{4.15}$$

so that

$$c(L) = -\Delta Q \sum_{n=-\infty}^{\infty} (e^{-|4nW+2L|} - e^{-|4nW+L|}). \tag{4.16}$$

To look at wave steepening, consider that

$$\frac{\partial c}{\partial L} = -\Delta Q \left[(e^{-L} - 2e^{-2L}) + (2e^{2L} - 2e^{-2L} + e^{-L} - e^{L}) \sum_{n=1}^{\infty} e^{-4nW} \right]. \tag{4.17}$$

For our case of a right-hand wedge with $\Delta Q < 0$, (4.17) indicates that

$$\frac{\partial c}{\partial L} < 0 \quad \text{for small } L, \text{ large } W,$$

$$\frac{\partial c}{\partial L} > 0 \quad \text{for sufficiently small } W.$$

Hence a right-hand intrusion in a wide channel would be expected to rarefy, whereas such an intrusion in a sufficiently narrow channel is expected to steepen. This in fact is the observed behaviour for the leading edge of the pinched-off quantity of fluid on the right-hand wall in the narrow ($2W = 1$) channel case, versus the very narrow ($2W = 0.2$) channel. The former retains a thin wedge at its leading tip, whereas the latter steepens into a blunt nose (compare figures 13 and 16). Note also that the shear of the Gill solution is small across the pinched-off fluid in these cases, and hence not a major perturbation to the u, v of (4.14), (4.15).

For very wide channels, the limit of the Gill solution is simply

$$u_{\text{Gill}} = \Delta Q e^{-L}. \tag{4.18}$$

When this flow is added to the large-W limit for u in (4.14), the sign of $c(L)$ changes from negative to positive, but the implied rarefaction still obtains. For a large-scale perturbation on the front in the centre of a very wide channel, application of (4.10) (interchanging x- and y-directions) without including the interior Gill solution yields a non-zero value for $c(M)$, where M represents the distance from the front to the y'-axis. However, inclusion of the Gill solution, which is centred on the y'-axis, cancels out this propagation tendency, yielding

$$c(M) = 0. \tag{4.19}$$

This serves to re-emphasize how the placement of the y'-axis for the Gill solution is completely arbitrary; were it not, the value of $c(M)$ would be dependent upon such placement. Further, the exact cancellation of the relevant contour- and Gill-contributions reminds us that at any time the flow field (and surface displacement) far away from the boundaries is simply that obtained by linear geostrophic adjustment of a line of surface discontinuity coinciding with the Q front.

4.3. *Processes as a function width*

Both left- and right-hand sides of the channel exhibit considerably different behaviour in very wide versus narrow cases. Overall, the left-hand wedge advances furthest with respect to the central portion of the front in the wide channel case, whereas the right-hand wedge pinches off from the central portion most quickly in the very narrow channel case. These effects are a function of the strength of communication possible between the two walls, and the degree of influence of rotation on the dynamics. The similarity among the initial evolution of the very wide (25λ and 10λ) and intermediate width (5λ) channels suggests that, given sufficient time, the right-hand wedge may pinch off and the central region of the channel will come up to speed with the left-hand wedge. If this reasoning is correct , then we have established that at any finite value of x the high potential vorticity fluid will eventually all have washed down the channel. This strongly suggests that the low potential vorticity, 'left-hand jet' of the upstream region will eventually propagate itself down the channel. In the case of the very narrow channel, results should be similar to those which would have been obtained for a non-rotating channel. In fact the ejected mass of fluid, with its noselike leading edge, bears at least a superficial resemblance to the exact, permanent form elliptical eddies that propagate along walls in the rigid lid case (Saffman & Tanveer 1982).

The time required for the high potential vorticity fluid to wash down the channel increases rapidly as a function of channel width. As a useful diagnostic of this tendency, we calculated the observed time τ' at which the most upstream portion of the high potential vorticity fluid had advanced at least one deformation radius downstream from its initial location. For widths $2W = 0..2$, 1.0, 5.0 and 10.0, observed values of τ' were approximately 1.01, 1.1, 5.0 and 50, respectively. This roughly exponential dependence of τ' on $2W$ suggests a value well in excess of $\tau' = 1000$ for $2W = 25$. Indeed, such downstream advancement was not observed for the considerably shorter run of the $2W = 25$ case described in §3.1. However, a longer run was attempted in which the right-hand wedge was not allowed to advance beyond $x' = 50$, to retain a sufficient density of points in the channel interior. Results indicate that the contour evolves into a single-lobed structure, as it did for the $2W = 10$ case (compare figures 19 and 9*a*). The left-hand side of this structure moves continually toward the right-hand side of the channel. Ultimately it is expected that, as for narrower channels, the lobe will move close enough to the right-hand wall for translation beyond the line $x = 0$ to occur.

It is significant to note that such steady solutions as are apparent in the narrower channels do not involve a single pattern which translates at constant speed. Rather, there exist both the central portion of the front and its associated flow pattern, which translate downstream at uniform velocity, and the coherent mass of lower potential vorticity fluid, which translates at a far greater velocity. This remarkable ejection of fluid appears to be a necessary step in the set-up of steady down-channel flow, and does not repeat within the time period of any of these simulations. It is conceivable that no such steady central pattern can exist for the wide channel case, until such time as this ejection on the right-hand wall occurs.

Stern (1986) examined the evolution of a nose of low potential vorticity fluid connected to a tail of uniform width against an isolated wall. He found the front separating the two fluid regions eventually deforms such that ambient fluid is engulfed by the nose. While this effect is quickest for a narrow fluid tail (e.g. within $\tau = 12$ for width 0.5λ), it is possible that such engulfment could occur (albeit more

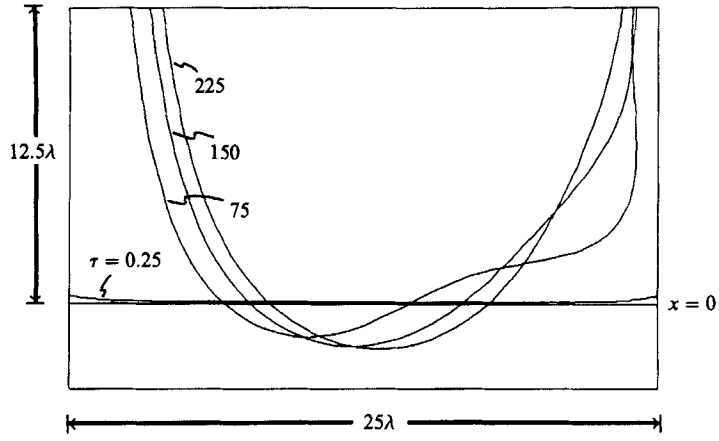

FIGURE 19. Evolution of the central portion of the potential vorticity front for a channel of width $2W = 25$ for $\tau = 0.25, 75, 150, 225$. The front is plotted in the fixed frame S, illustrating the long-time behaviour of the front near the origin $x = 0$.

slowly) for our considerably wider left-hand intrusion in the widest channel case. The communication between channel walls (which continues to deform the tail even at $\tau = 225$), may ultimately prevent this, however. The fact that such engulfment did not occur in any of the narrower channels probably results from the strong cross-channel communication in these cases, and consequent failure to form a nose on the left-hand wall. In the limit of infinite channel width, where cross-channel communication and consequent washout are prohibited, such effects might become evident as the left-hand nose moves ever further beyond the stationary central portion of the contour.

4.4. *Self-advection and down-channel flux*

In the widest channel case, the left-hand nose moves along the wall in a manner not attributable to inertial overshoot alone. Rather, the nose of uniform potential vorticity fluid behaves in a manner consistent with the self-advection of a point vortex of negative sign near a wall. This effect was formalized in (4.7) for a wedge of uniform potential vorticity fluid against an isolated wall. Considering a mean angle of $-\frac{1}{4}\pi$ of the nose within 1λ of its leading tip (see figure 4), (4.7) suggests a self-advection velocity of 0.29. This compares favourably with the observed advection rate of 0.25, despite the curvature of the actual contour relative to a straight wedge. Hence, while inertial overshoot serves initially to create a nose of low potential vorticity fluid on the left-hand wall, it is vortex self-advection which best explains the persistent creep of that fluid along the wall.

The possiblity of sustained self-advection of new (low potential vorticity) fluid down-channel on the left-hand wall suggests a significant flux of new fluid in that direction, relative to the amount streaming down-channel on the right-hand wall. Consider the cross-channel integral of down-channel flux in either half of the channel:

$$F_{\mathrm{L}}(x) = \int_0^W u(x,y)\,\mathrm{d}y = \eta(x,W) - \eta(x,0), \tag{4.20}$$

$$F_{\mathrm{R}}(x) = \int_{-W}^0 u(x,y)\,\mathrm{d}y = \eta(x,0) - \eta(x,-W). \tag{4.21}$$

Initially (at $\tau = 0$) the height $\eta(0, y)$ is antisymmetric with the boundary values $\pm \tanh W$ (see (2.23)). Hence

$$F_L(0) = F_R(0) = \tanh W. \tag{4.22}$$

At $\tau = 0$ this fluid consists entirely of new fluid, but for $\tau > 0$ or $x \neq 0$ this will not generally be the case. The ultimate configuration of $\eta(0, y)$ for $\tau \gg 0$ suggested in figure 9 corresponds to:

$$F_L(0) = 2 \tanh W \quad F_R(0) = 0. \tag{4.23}$$

For intermediate times and locations $x \neq 0$, the relative fluxes $F_L(x)$, $F_R(x)$, and the fraction of each of those fluxes which is new fluid, must be determined from the numerical experiments. A plot of new and total (old plus new) fluid flux at $\tau = 25$ in the very wide ($2W = 25$) channel case is shown in figure 20. Flux of new fluid decreases monotonically in x on both sides of the channel, as the nose and wedge regions narrow. At $x = 0$, the down-channel flux of new fluid in the left-hand portion of the channel is equal to or greater than its counterpart in the right-hand region. This attests to the power of the self advection dynamics, which continue to draw fluid up the left-hand boundary long after the linear adjustment has taken place.

4.5. *Strongly nonlinear cases*

Though the contour dynamical algorithm used here is convenient for small amplitude, inviscid motions it cannot be employed for strongly nonlinear ($\epsilon \gg 0$) dynamics. As a check on the relevance of our contour dynamical results to such a strongly nonlinear case, we compared results for the intermediate channel width with results from a primitive equation model using the fully nonlinear shallow-water equations. While the shallow-water model precludes deep-water dispersive effects which must arise for very large amplitudes, such effects are considered a minor perturbation on the advective evolution which is our primary focus here. The staggered grid of Sadourney (1975) was employed for the numerical integration. This scheme has the desirable property of enstrophy conservation at small amplitudes. Initial conditions in the primitive equation model mimicked the initial conditions of the Gill problem, with a state of rest everywhere and a discontinuity in surface height spanning the channel at $x = 0$. As with other primitive equation models, it was necessary to include a non-trivial damping term (Laplacian friction in this case). To eliminate the resulting leakage of relative vorticity from the walls, a 'superslip' boundary condition was employed for the channel walls (normal gradient of relative vorticity = 0 at each wall). Runs with a 'no-slip' boundary condition on each wall were also tested, to ascertain how boundary friction (e.g. as experienced in laboratory experiments) would affect the results. In each case, the radiation boundary condition of Camerlengo & O'Brien (1980) was employed for the ends of the channel.

Results at $\tau = 5.0$ are compared in figure 21 (a, b) for the contour dynamical run ($\epsilon \to 0$) *vs.* a strongly nonlinear primitive equation, 'superslip' run ($\epsilon = 0.33$) in a channel where $2W = 5$. Agreement is strikingly good for both the location of the potential vorticity boundary (smeared out by Laplacian friction in the primitive equation case) and the velocity field, although the fluid in the centre of the channel has translated further downstream in the $\epsilon = 0.33$ case. With a 'no-slip' boundary condition, potential vorticity is no longer well conserved near the walls (figure 21 c). The left-hand jet separates from that wall, defeating the tendency for downstream propagation of a left-hand 'nose' of new fluid, although the interior jet and interior fluid move steadily downstream as in the 'superslip' and contour dynamical runs.

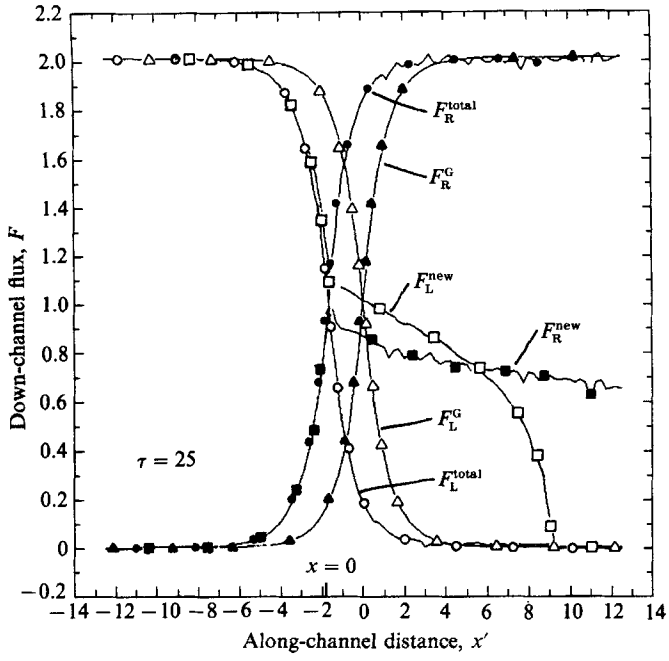

FIGURE 20. Down-channel fluxes of new (low potential vorticity) and total (old plus new) fluid in the left (F_L) and right (F_R) halves of the very wide ($2W = 25$) channel at $\tau = 25$, as a function of the down-channel coordinate x' in the moving frame S'. The position of $x = 0$ in the fixed frame S is indicated. Shown for comparison are the fluxes in the left and right halves due to the advected Gill solution (F_L^G and F_R^G, respectively).

Another technique for exploring the behaviour of the primitive equations runs, relative to their contour dynamical counterparts, is to track the positions of an initially square array of Lagrangian floats. Although it is recognized that properties such as potential vorticity will not be exactly conserved following a Lagrangian drifter when Laplacian friction is present, such floats can serve as a useful marker of the path of the new (lower potential vorticity) fluid in the present case. Float maps in this context must be interpreted with caution, as successive strings of floats are advected out from their initial locations, leaving no marker for the subsequent fluid there.

Figure 22 exhibits the float tracks for the 'superslip' version of the $2W = 5$ case, with the equivalent values of τ. Floats are placed such that all lie in the region of new fluid, just below the line $x = 0$. Note especially how the new fluid, after travelling down-channel along the right-hand wall, pinches off in a manner similar to that seen in figure 11 (note different x-scales in these two figures). Float markers rapidly disappear from the left-hand wall; hence the fluid front is more difficult to track in this region (although one float string does apparently serve this purpose). For the narrow channel 'superslip' case (figure 23), only small values of τ can be achieved before the entire float array is swept out of the downstream (radiating) boundary of the model domain. However, such deformation as is apparent by $\tau = 2.7$ is quite consistent with that on the right-hand wall in figure 13.

The float maps for the wide channel ($2W = 25$) 'superslip' case (figure 24*a*) nicely confirm the penetration of new fluid on both left- and right-hand walls up to $\tau = 41$, beyond which time the sparseness of floats becomes a problem. It is especially important not to interpret the subsequent evolution of the right-hand side as

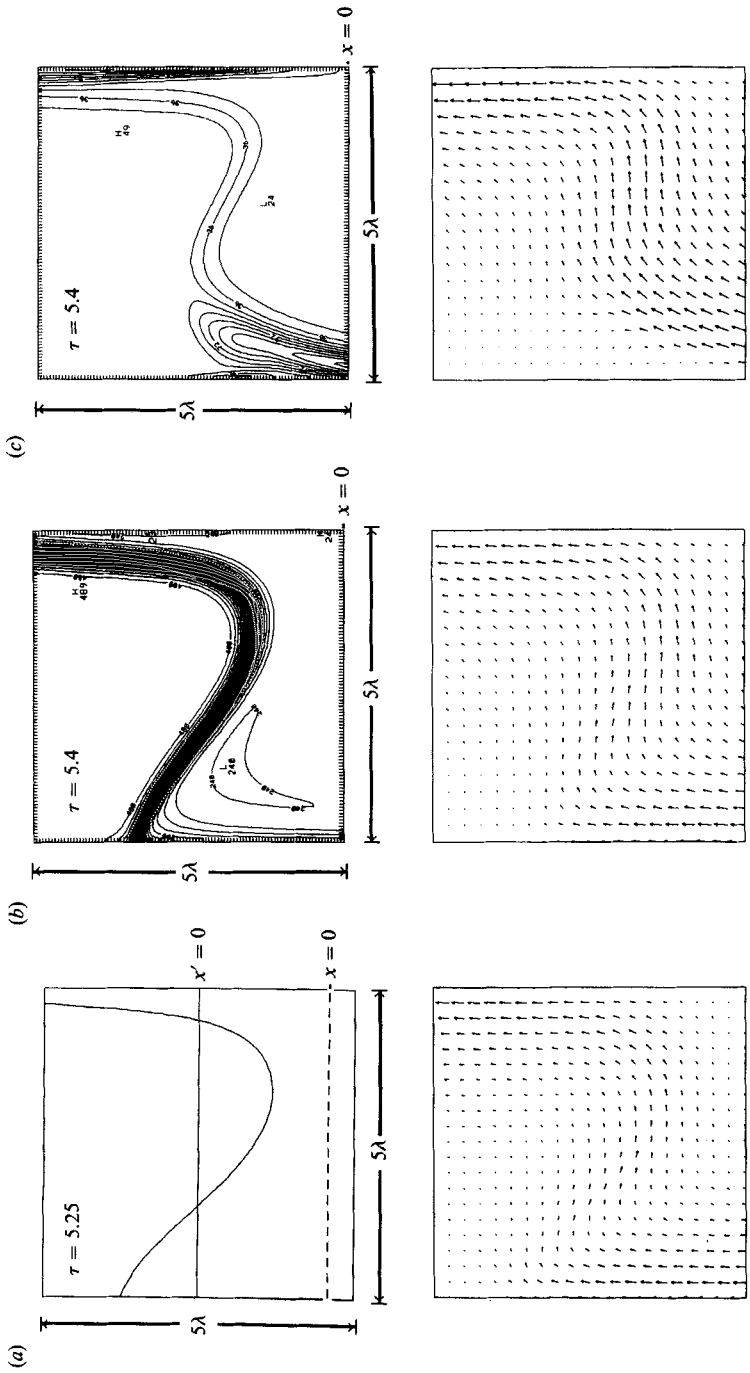

FIGURE 21. Comparison of (*a*) contour dynamical run for the intermediate width channel ($\epsilon \to 0$, $2W = 5$); (*b*) strongly nonlinear primitive equation run for that channel ($\epsilon = 0.33$); (*c*) strongly nonlinear primitive equation run with boundary friction ('no-slip' boundary condition).

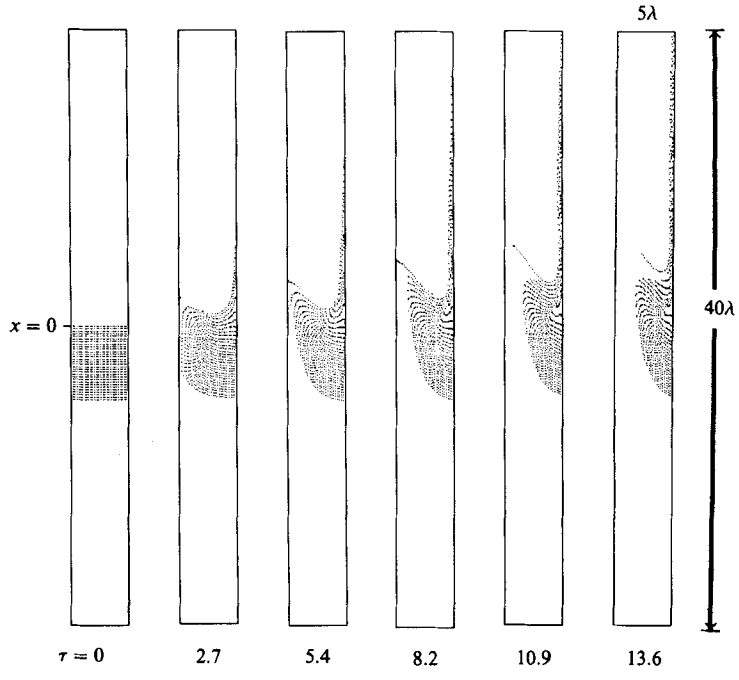

FIGURE 22. Evolution of an initially square array of Lagrangian floats in the intermediate width ($2W = 5$) channel primitive equation run.

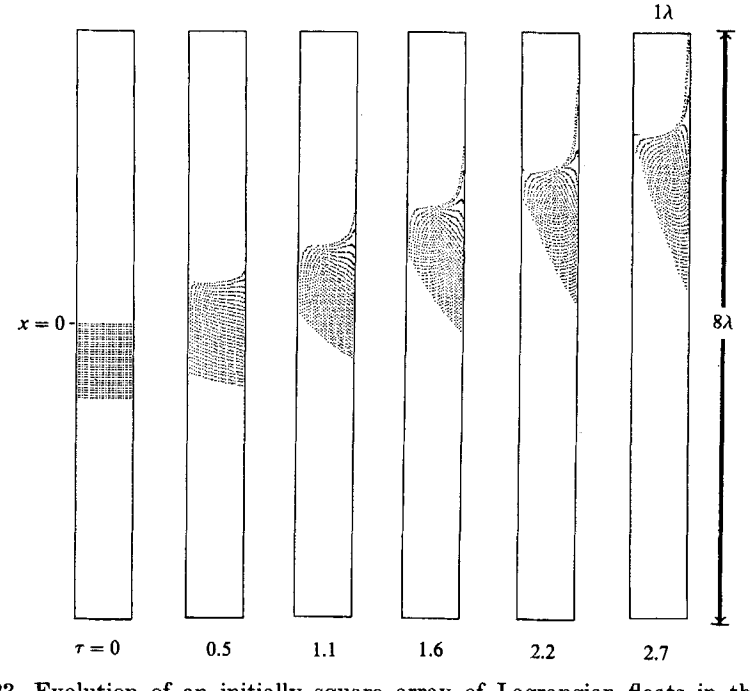

FIGURE 23. Evolution of an initially square array of Lagrangian floats in the narrow width ($2W = 1$) channel primitive equation run.

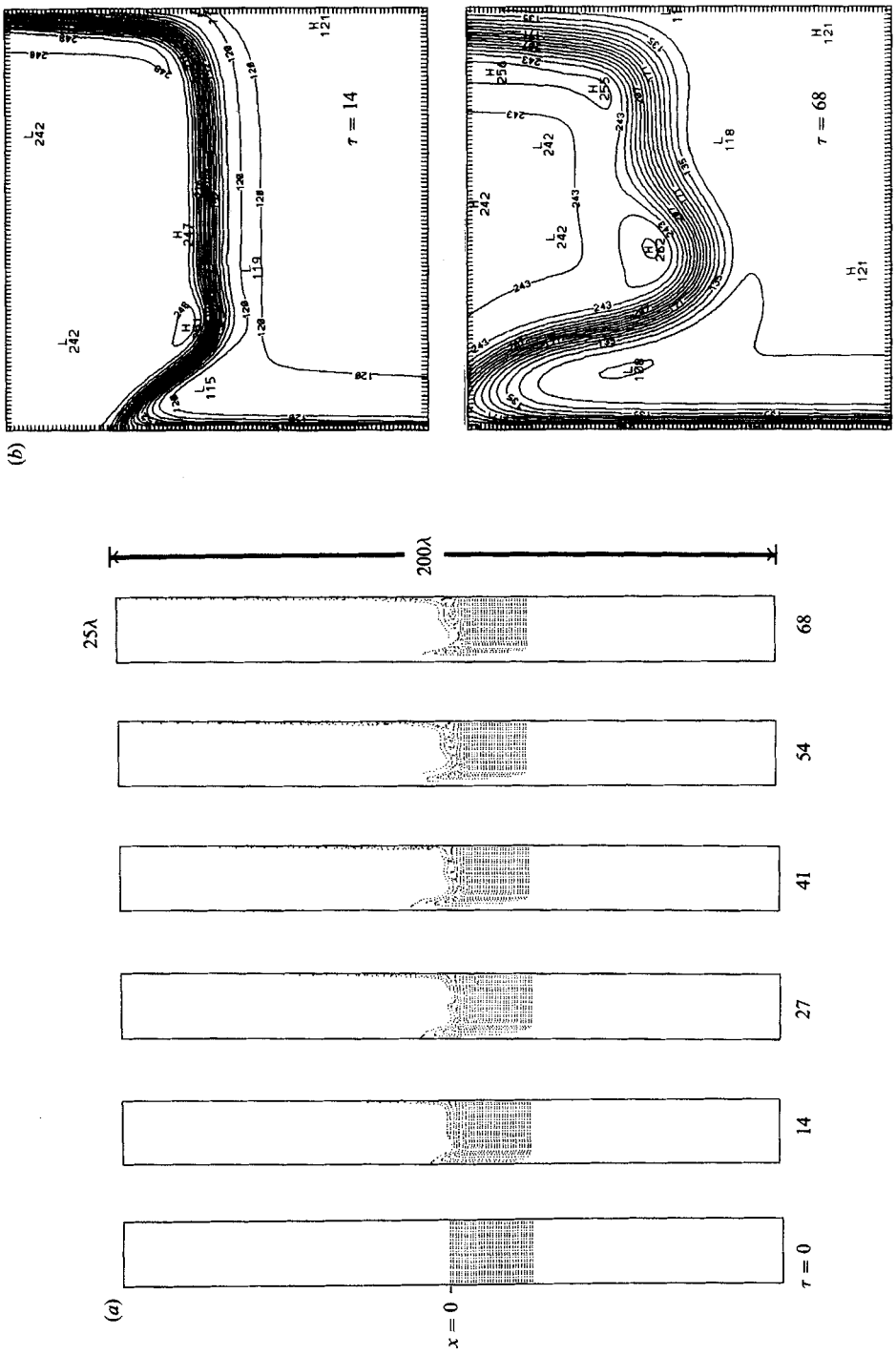

FIGURE 24. (a) Evolution of an initially square array of Lagrangian floats for the very wide ($2W = 25$) channel primitive equation run. (b) Contours of potential vorticity at $\tau = 14$ and $\tau = 68$ are shown for comparison.

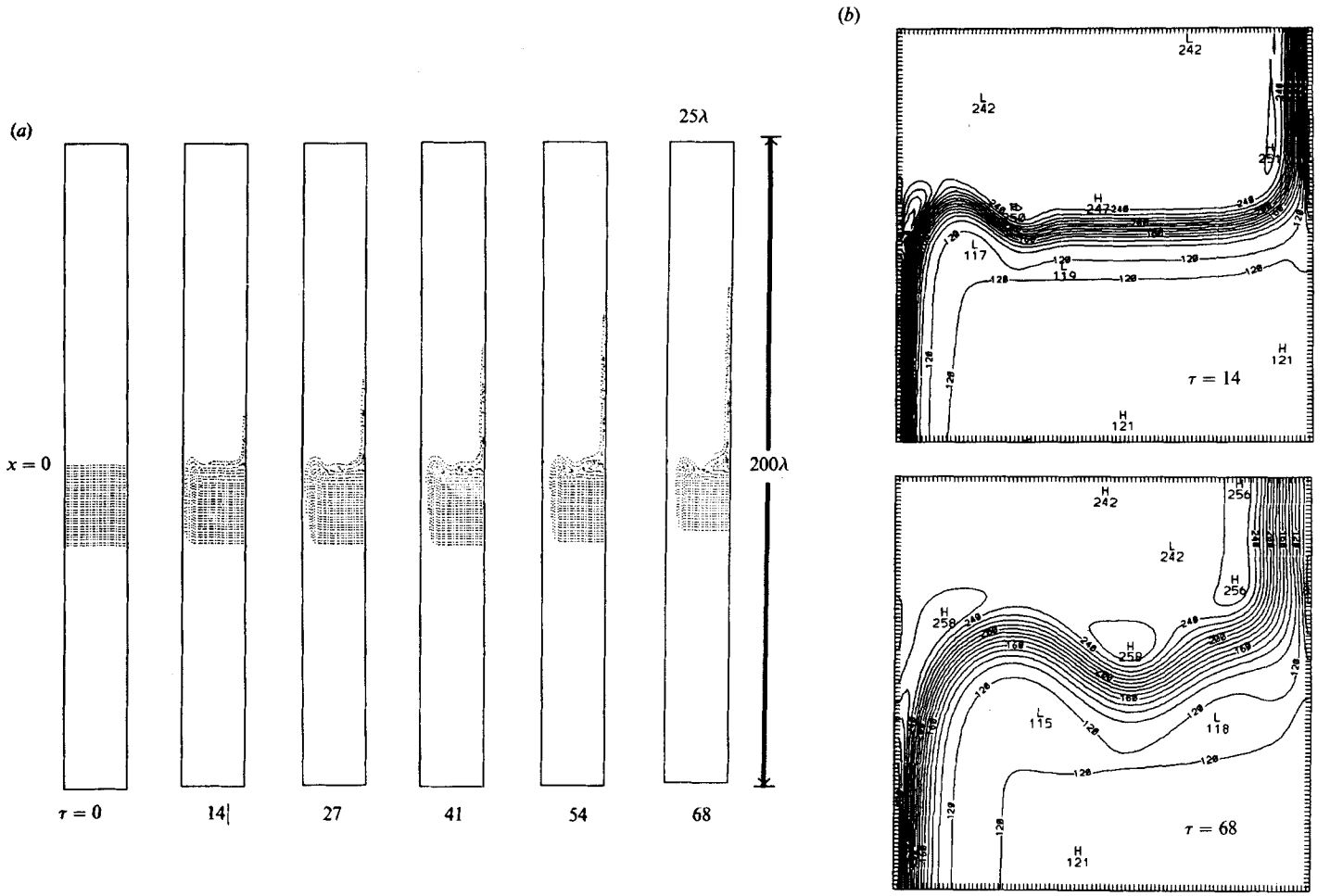

FIGURE 25. (*a*) Evolution of an initially square array of Lagrangian floats for the very wide ($2W = 25$) channel primitive equation run with boundary friction ('no-slip' condition). (*b*) Contours of potential vorticity at $\tau = 14$ and $\tau = 68$ are shown for comparison.

'pinching-off' behaviour (as for the $2W = 5$ case), as the reduced width of the float-rich area on the right-hand wall near the origin is merely an artifact of the limited number of floats available to track new fluid. Contour maps of potential vorticity at $\tau = 14$ and $\tau = 68$ (figure 24*b*) confirm similar behaviour of the potential vorticity front to that shown in figures 4 and 19 for the contour dynamical runs.

A final set of float maps illustrates the dramatic effect of a 'no-slip' boundary condition on the primitive equation run for the $2W = 25$ case (figure 25*a*). Not only is the penetration of new fluid on the left-hand wall defeated, but such penetration on the right-hand wall is considerably slowed relative to the 'superslip' or contour dynamical (inviscid) case. The right-hand wedge acquires strong negative values of relative vorticity, as evidenced by the slow advance of the floats near the wall. Again, contours of potential vorticity at selected times are exhibited for comparison (figure 25*b*). They reveal a pattern with limited conservation of potential vorticity near each wall and arrested penetration of the left-hand front. Overall, these diffusive effects result in a velocity structure which is markedly different from that of the inviscid runs, and is more similar to that of the linearly adjusted state.

In the limit of $\epsilon \to 1.0$, no shallow water run is possible as the fluid thickness for $x > 0$ vanishes. In this case the leading wave and fluid fronts must be coincident, and a true gravity current would evolve on the right-hand wall. It is unclear precisely how the wedgelike and noselike intrusions reported here relate to the 'wedge' and 'bore' similarity solutions offered by Stern, Whitehead & Hua (1982) for a boundary-trapped gravity current. However, such an idealized gravity current should have negative relative vorticity (i.e. stronger down-channel flow away from the wall), just as was found for the new fluid intrusions in our contour dynamical runs. Hence we have explored a dynamical regime with elements of both Kelvin wave and boundary-trapped gravity current dynamics, the latter serving as an intermediate step before a final configuration of surface height and velocity is established.

5. Conclusions

Steady flows in a channel have, at one extreme, hydraulics models and, at the other, models involving 'arrested waves'. Hydraulics assumes normally that all of the 'upstream' fluid washes down the channel, carrying with it the effect of upstream boundary conditions, and establishing a steady flow. Wave models conversely assume that flow pathways are determined by group velocity, and the developed flow may occupy only a small fraction of the width of the domain. Slow ($\gg f^{-1}$) advective adjustment can result in the evolution of fluid states intermediate between those considered by linear wave and hydraulic models. For the case of a wide ($\gg \lambda$) rotating channel with an initial step discontinuity in surface height, such nonlinear effects are capable of transporting fluid along both walls, rather than just the one supporting a downstream travelling Kelvin wave. In narrower channels ($\sim \lambda$) a very narrow ($\ll \lambda$), coherent mass of low potential vorticity fluid is shot downstream ahead of its source. Ultimately the low potential vorticity fluid is expected to wash downstream all across the channel for arbitrary channel width (here demonstrated for widths up to 10λ), i.e. the two walls of the channel must eventually communicate with one another. The time required for significant communication appears to increase exponentially with channel width. Such adjustments appear even in strongly nonlinear cases, where the advective motions occur on timescales of order f^{-1}. The destruction of vorticity near each wall by friction and diffusion can make drastic changes to these conclusions, defeating especially the transport of fluid along

that wall not supporting a downstream travelling Kelvin wave. It is probably this feature, along with the impressive short-time behaviour of the linear wave adjustment, that dominates the numerical and laboratory experiments in the literature.

Acknowledgements. A. J. H. was supported by the Office of Naval Research through contract N000 14-87-K-0160. P. B. R. was supported by National Science Foundation grant OCE-86-13725. We gratefully acknowledge the support of the San Diego Supercomputer Center.

Appendix. Determination of the free-surface elevation of the wave-adjusted flow

The free-surface elevation of the wave-adjusted steady state satisfies

$$\nabla^2\eta_0 - \eta_0 = \operatorname{sgn} x \quad (|y| < W), \tag{A 1}$$

$$\eta_0 = \tanh W \quad (y = +W). \tag{A 2}$$

Define the asymptotic but discontinuous particular solution

$$\begin{aligned}\eta^* &= \begin{cases} -1 + \operatorname{sech} W\, \mathrm{e}^{-y} & (x > 0), \\ 1 - \operatorname{sech} W\, \mathrm{e}^{y} & (x < 0), \end{cases} \\ &= -\sinh y \operatorname{sech} W + \operatorname{sgn} x(-1 + \cosh y \operatorname{sech} W). \end{aligned} \tag{A 3}$$

Then $\eta \sim \eta^*$ for $|x| \gg 1$. Write $\eta_0 = \eta^* + p$, so p satisfies the homogeneous forms of (A 1) and (A 2). Since η_0 and $\partial\eta_0/\partial x$ are continuous across $x = 0$, p_x is continuous and

$$[p] = -[\eta^*] = 2 - 2\operatorname{sech} W \cosh y, \tag{A 4}$$

where [ ] denotes the jump in the enclosed quantity across $x = 0$. As $[\eta^*]$ is even in y and vanishes at $y = W$, it possesses a Fourier cosine expansion with only the odd terms appearing, namely,

$$-[\eta^*] = \frac{4}{W} \sum_{m=0}^{\infty} \frac{(-1)^m \cos a_m y}{a_m(1 + a_m^2)}, \tag{A 5}$$

where $a_m = (m + \frac{1}{2})\pi/W$. Thus

$$p = \frac{2}{W} \operatorname{sgn} x \sum_{m=0}^{\infty} \frac{(-1)^m}{a_m(1 + a_m^2)} \cos(a_m y) \exp[-(1 + a_m^2)^{\frac{1}{2}}|x|]. \tag{A 6}$$

Adding η^* gives the form of η_0 quoted in (2.20).

REFERENCES

Baines, P. G. 1980 The dynamics of the southerly buster. *Austral. Met. Mag.* **28**, 175–200.

Beardsley, R. C., Dorman, C. E., Friehe, C. A., Rosenfeld, L. K. & Winant, C. D. 1987 Local atmospheric forcing during the coastal ocean dynamics experiment. I. A description of the marine boundary layer and atmospheric conditions over a northern California upwelling region. *J. Geophys. Res.* **92**, 1467–1488.

Blumen, W. 1972 Geostrophic adjustment. *Rev. Geophys. Space Phys.* **10**, 485–528.

Camerlengo, A. L. & O'Brien, J. J. 1980 Open boundary conditions in rotating fluids. *J. Comput. Phys.* **35**, 12–35.

Csanady, G. T. 1976 Topographic waves in Lake Ontario. *J. Phys. Oceanogr.* **6**, 93–103.

Dorman, C. 1987 Possible role of gravity currents in northern California's coastal summer wind reversals. *J. Geophys. Res.* **92**, 1497–1506.

GILL, A. E. 1976 Adjustment under gravity in a rotating channel. *J. Fluid Mech.*, **77**, 603–621.

GILL, A. E. 1977*a* Coastally trapped waves in the atmosphere. *Q. J. R. Met. Soc.* **103**, 431–440.

GILL, A. E. 1977*b* The hydraulics of rotating channel flow. *J. Fluid Mech.* **80**, 641–671.

GILL, A. E. 1982 *Atmosphere–Ocean Dynamics*, ch. 7, 10. Academic.

GILL, A. E., DAVEY, M. K., JOHNSON, E. R. & LINDEN, P. F. 1986 Rossby adjustment over a step. *J. Mar. Res.* **44**, 713–738.

GODFREY, J. S. 1989 A Sverdrup model of the depth-integrated flow of the world ocean allowing for island circulations. *Dyn. Atmos. Ocean.* in press.

HERMANN, A. J., HICKEY, B. M., MASS, C. F. & ALBRIGHT, M. 1989 Orographically-trapped wind events in the Pacific Northwest and their oceanic response. Submitted to *J. Geophys. Res.*

JOHNSON, E. R. 1985 Topographic waves and the evolution of coastal currents. *J. Fluid Mech.* **160**, 499–509.

KAWASE, M. 1987 Establishment of deep ocean circulation driven by deep-water production. *J. Phys. Ocean.* **17**, 2294–2317.

KILLWORTH, P. D. 1987 A note on van Heijst and Smeed. *Ocean Modelling* **69**, 7.

LIGHTHILL, M. J. 1967 On waves generated in dispersive systems by travelling forcing effects, with applications to the dynamics of rotating fluids. *J. Fluid Mech.* **27**, 725–752.

LORENZ, E. N. & KRISHNAMURTHY, V. 1987 On the nonexistence of a slow manifold. *J. Atmos. Sci.* **44**, 2940–2950.

MASS, C. & ALBRIGHT, M. 1987 Coastal southerlies and alongshore surges of the west coast of North America: Evidence of topographically trapped response to synoptic forcing. *Mon. Weather Rev.* **115**, 1707–1738.

MIDDLETON, J. F. 1987 Energetics of linear geostrophic adjustment. *J. Phys. Ocean.* **17**, 735–740.

ROSSBY, C. G. 1937 On the mutual adjustment of pressure and velocity distributions in certain simple current systems. I. *J. Mar. Res.* **1**, 15–28.

ROSSBY, C. G. 1938 On the mutal adjustment of pressure and velocity distributions in certain simple current systems. II. *J. Mar. Res.* **2**, 239–263.

SADOURNEY, R. 1975 The dynamics of finite-difference models of the shallow-water equations. *J. Atmos. Sci.* **32**, 680–689.

SAFFMAN, P. G. & TANVEER, S. 1982 The touching pair of equal and opposite uniform vortices. *Phys. Fluids* **25**, 1929–1930.

STERN, M. E. 1985 Lateral wave breaking and 'shingle' formation in large-scale shear flow. *J. Phys. Ocean.* **15**, 1274–1283.

STERN, M. E. 1986 On the amplification of convergences in coastal currents and the formation of 'squirts'. *J. Mar. Res.* **44**, 403–421.

STERN, M. E. 1987*a* Horizontal entrainment and detrainment in large-scale eddies. *J. Phys. Ocean.* **17**, 1688–1695.

STERN, M. E. 1987*b* Large-scale lateral entrainment and detrainment at the edge of a geostrophic shear layer. *J. Phys. Ocean.* **17**, 1680–1687.

STERN, M. E., WHITEHEAD, J. A. & HUA, B. 1982 The intrusion of a density current along the coast in a rotating fluid. *J. Fluid Mech.* **123**, 237–265.

ZABUSKY, N. J., HUGHES, M. H. & ROBERTS, K. V. 1979 Contour dynamics for the Euler equations in two dimensions. *J. Comp. Phys.* **30**, 96–106.